Karlsruhe Institute of Technology

Institute of Fluid Mechanics

Direct numerical simulation of controlled turbulent duct flows

Master Thesis of

Steffen Straub

At the Department of Mechanical Engineering,
Institute of Fluid Mechanics

Advisors: Prof. Dr.-Ing. Bettina Frohnapfel
M. Sc. Davide Gatti
Ph.D., Docent Philipp Schlatter
Ph.D. Ricardo Vinuesa

Duration: June 2015 – October 2015

Acknowledgements

I would like to thank Bettina Frohnapfel and Philipp Schlatter for giving me the possibility to do this thesis at KTH in Stockholm. Furthermore, I need to thank Davide Gatti and Ricardo Vinuesa for their support during the last months.

I would like to thank both the Professor Dr.-Ing. Erich Müller-Stiftung and the Dr.-Ing Willy-Höfler-Stiftung for granting me their scholarship.

This research was conducted using the resources provided by the Swedish National Infrastructure for Computing (SNIC) at High Performance Computing Center North (HPC2N) and at National Supercomputer Centre (NSC) at Linköping University.

I declare that I have developed and written the enclosed thesis completely by myself, and have not used sources or means without declaration in the text.

Karlsruhe, 06.10.2015

.....

(**Steffen Straub**)

Abstract

Direct numerical simulations of controlled turbulent duct flows are conducted with the spectral element code Nek5000 (Fischer et al., 2008). The applied control technique is the harmonic oscillation of the horizontal walls in order to achieve turbulent drag reduction. To the best of the author's knowledge, this is the first time that this control technique is numerically investigated in a duct geometry, which is a standard choice in experiments. Different control parameters, namely the amplitude of wall velocity and the controlled area, are tested in three different cases and their results are compared to each other and to the uncontrolled flow. Two effects of this control technique in a rectangular duct are investigated: the effect on drag reduction and the effect on the secondary motions induced by the corners. Additionally, selected statistics of the mean flow are evaluated in order to understand the impact of the moving walls on the turbulent flow.
It is found that the secondary motions are strongly amplified and modified in shape and location compared to the uncontrolled turbulent duct flow. One of the two counter rotating streamwise vortices at the corner is strengthened and pushes the other one closer to the core region. In the case of partially moving horizontal walls an additional pair of counter rotating streamwise vortices is generated.
The achieved drag reduction levels are poor compared to the results in a channel. The only positive drag reduction achieved is 3% in one case where the corresponding results in the channel are 19%. The case with higher amplitude of wall velocity shows a drag increase of 10% and the case with reduced controlled area only in the centre of the duct yields drag increase of 1%. It is shown that these low or even negative levels of drag reduction are a result of the poor performance at the sides of the controlled region.

Direkte numerische Simulationen von kontrollierten turbulenten Strömungen werden im Kanal unter Berücksichtigung der Seitenwände mit dem spectral element code Nek5000 Fischer et al. (2008) durchgeführt. Die verwendete Technik zur Strömungskontrolle ist die harmonische Oszillation der horizontalen Wände zum Zwecke der Reduktion der turbulenten Reibung. Nach bestem Wissen des Autors ist dies das erste Mal in der diese Technik zur Strömungskontrolle in in einem Kanal mit Seitenwänden numerisch untersucht wird. Verschiedene Parameter der Strömungskontrolle, und zwar die Wandgeschwindigkeitsamplitude und die kontrollierte Fläche, werden in drei unterschiedlichen Fällen getestet und ihre Ergebnisse untereinander und mit dem unkontrollierten Fall verglichen. Zwei Effekte dieser Technik zur Strömungskontrolle im rechteckigen Kanal mit Seitenwänden werden untersucht: der Effekt auf die Reibungsminderung und der Effekt auf die Sekundärströmungen, welche durch die Ecken im Kanal erzeugt werden. Zusätzlich werden einige gemittelte Statistiken ausgewertet um die Auswirkung der bewegten Wände auf die turbulente Strömung zu verstehen.
Die Sekundärströmung wird verglichen zum unkontrollierten Fall stark angefacht und in Gestalt und Lage verändert. Einer der entgegengesetzt rotierenden Wirbeln in der Ecke wird verstärkt und verdrängt den anderen Wirbel näher ins Zentrum des Kanals. Im Falle von nur teilweise kontrollierten horizontalen Wänden wird ein weiteres Paar von entgegengesetzt rotierenden Wirbeln erzeugt.
Das erzielte Niveau der Reibungsminderung ist verglichen zu den Ergebnissen im Kanal ohne Seitenwände sehr gering. Die einzige positive Reibungsminderung, die erreicht wird beträgt 3% in einem Fall bei dem 19% im Kanal ohne Seitenwände erreicht wird. Der Fall mit höherer Wandgeschwindigkeitsamplitude ergibt eine Reibungserhöhung von 10% und im Falle verkleinerter Fläche der Strömungskontrolle nur im Zentrum des Kanals ergibt sich eine Reibungserhöhung von 1%. Es wird gezeigt, dass diese niedrigen oder sogar negativen Werte der Reibungsminderung ein Resultat der schlechten Performance an den Seiten des kontrollierten Gebiets sind.

Contents

1. Introduction

1.1. Motivation

Our daily life is surrounded by many different kinds of wall-bounded flows. This could be for instance the flow around a car, bus, metro or any other means of transportation. If you go on vacation and take the plane, the flow around its wings is the crucial factor which enables the plane to fly. Another example is the flow through pipes. There are huge pipelines for the transportation of gas, oil or water for instance. All those flows and many more have one thing in common: they produce drag.
For some cases the drag is beneficial or even essential, as for example for a parachute, but for many other flows drag is an unwanted by-product. Modern vehicles such as cars, planes or ships do not produce as much drag as they did in the beginning of their development. For those applications, as for flow through pipelines, less drag often means less power consumption. For instance, if one applies a specific pressure gradient to push fluid through a section of a pipe, the same mass flow rate can be achieved with a smaller pressure gradient when drag is reduced. On the other hand drag, reduction can also result in an increased mass flow rate by keeping the pressure gradient constant. In both cases the results are beneficial. Reducing the power input or increasing the mass flow rate in the example above leads to a higher efficiency of the device. A higher efficiency is not only beneficial in a financial point of view but it improves ecological aspects, too. Kim (2011) claims that we could save 38 billion Dollar per year if the fuel consumption of worldwide shipping was reduced by 30 % (considering 2003 figures of fuel consumption and 60 Dollar per barrel). A reduction of fuel consumption would also reduce exhaust gases and carbon dioxide.
This is where the science of flow control comes in (Gad-el Hak, 2000). In this branch of fluid dynamics one tries to manipulate the natural behaviour of the flow in a beneficial way (Pope, 2010). For instance, improved mixing between fluids, improved heat transfer or methods for drag reduction are investigated. The focus of this thesis is on a simple technique for drag reduction. Since most engineering flows are turbulent, the goal is to reduce turbulent drag.
One can distinguish between laminar and turbulent flows. The cases considered here are turbulent flows. It is difficult to give a proper definition of turbulence. Some of its characteristics however can help to clarify its meaning.

According to Tennekes and Lumley (1972) they are:

- Irregularity, randomness
- Mixing: increased rates of momentum, heat and mass transfer
- Large Reynolds number
- Three-dimensional vorticity fluctuations: turbulent flows are rotational
- Dissipation: energy is needed to sustain turbulence
- Continuum: smallest scales are still larger than molecular length scales
- Turbulence is a feature of the flow not the fluid

A simple, yet imperfect definition of turbulence is given by Kundu et al. (2012) as "a dissipative flow state characterized by nonlinear fluctuating three-dimensional vorticity". Due to the mentioned characteristics of increased mixing and dissipation, usually turbulent flows are accompanied by higher drag compared to laminar flows. This additional component of drag for turbulent flows is referred to as turbulent drag.

1.2. State of the art

The different kinds of drag reduction mechanisms for wall-bounded flows can be grouped into either active or passive techniques (Gad-el Hak, 2000). The difference between those is that the former needs additional power input and the latter does not. For active techniques one can further differentiate between techniques which measure specific flow quantities and change their parameters accordingly (reactive) and techniques which do not react on changes in the flow (predetermined).
A well known passive technique for drag reduction is the use of riblets. This technique, which is inspired by the microgrooves of shark skin, has been shown to reach drag reduction levels of about 10 % (Bechert et al., 1997; Garcia-Mayoral and Jimenéz, 2011). For a wing-body Viswanath (2002) found $2-3\%$ total drag reduction based on limited wind tunnel data. One major advantage of passive techniques is that no additional power input is needed. However, the amount of drag reduction achieved so far is much smaller compared to active techniques. Predetermined active techniques do not require complex sensors and actuators as the reactive techniques do. They are simpler and cheaper than the reactive techniques.
One promising predetermined active control technique to reduce drag in channel and pipe flows is the spanwise oscillatory motion of the walls. This technique will be investigated in the present thesis. Jung et al. (1992) were the first to investigate this phenomenon by direct numerical simulations. They found that sustained turbulent drag reduction of 10 % to 40 % compared to the uncontrolled case was possible. Since then many experimental and numerical studies have been conducted to achieve a better understanding of the mechanisms behind this phenomenon. Laadhari et al. (1994) were able to show experimentally the effects of a spanwise oscillating wall for turbulent boundary layers. Their results are generally in good agreement with Jung et al. (1992). The first of many articles published by Quadrio and co-workers (Baron and Quadrio, 1995) confirms Jung et al. (1992)'s findings of 40 % drag reduction. They also take into account the power input needed to generate the wall motion and show that potential overall savings are possible. A simple model is proposed which states that the spatial coherence between streamwise vortices and low-speed streaks is disrupted causing the drag reduction. In another experimental investigation Choi et al. (1998) confirmed the previous results by achieving 45 % drag reduction in their wind-tunnel experiment. They propose a conceptual model that explains the decrease of the mean velocity-gradient close to the wall by a net spanwise

vorticity generated by the periodic Stokes layer. A new parameter which combines the influence range and the acceleration of the Stokes layer was introduced by Choi and Xu (2002) to obtain a simple equation that allows to estimate drag reduction rates. Another article by Quadrio's group (Quadrio and Ricco, 2004) identifies the optimal values for wall velocity amplitude and time period for harmonic wall oscillation by a parametric study. They show their results in drag reduction maps. Further attempts to shed some light on the mechanism for skin-friction drag reduction were done by Ricco et al. (2012). They look at the mean energy balance, turbulent kinetic energy balance and the turbulent enstrophy balance to find one vorticity production term that is dominant and largely responsible for drag reduction. In a recent article Yakeno et al. (2014) claim that drag reduction is mostly due to suppression of ejection events by spanwise shear. Moreover, their results suggest a link between the suppression of ejection events and Ricco et al. (2012)'s vorticity production term.
Even though many experimental and numerical investigations have already been conducted the phenomenon behind this drag reduction technique is still not fully understood.

1.3. Objectives of this thesis

The objective of this thesis is to simulate the effects of the aforementioned flow control technique in a more realistic geometry than the standard plane channel. To the best of the author's knowledge all previous direct numerical simulations were done in such a channel with periodic boundary conditions in spanwise direction (and few simulations performed in boundary layers, for example Skote (2011); Lardeau and Leschziner (2013)). This artificial periodicity strongly simplifies the simulations. However, in experiments side walls need to confine the flow region.
Therefore, two different effects are being investigated. The first one is the effect of the side walls on the performance of the flow control technique. Gatti et al. (2015) find a discrepancy between their experimental results and results generated by direct numerical simulations which might be caused by not taking into account the effect of the side walls. The second one is the effect of the applied flow control technique on secondary motions produced at the duct corners. This mechanism is not present in the channel but in the duct and affects the mean flow (Vinuesa et al., 2014).
To be able to take the side walls into account a highly parallelized code using the spectral element method is used: Nek5000 (Fischer et al., 2008).

1.4. Structure of the thesis

After this introduction into the topic, chapter 2 presents the governing equations for incompressible fluid mechanics and the Reynolds-averaged Navier–Stokes equations as a general numerical method to tackle this set of nonlinear partial differential equations. Furthermore, the channel flow is investigated more closely and some specific features of the duct flow are mentioned. Finally, the applied control technique is presented.
Chapter 3 deals with the numerical methods used for the simulations in this thesis. The spectral element method is introduced with two model problems and the spatial and temporal discretization is shown. All the investigated cases are described in chapter 4. The setup for each channel and duct flow is described.
A comparison between data from the literature, a pseudo spectral code and results generated with the spectral element code Nek5000 is given in chapter 5 in order to validate the implementation of the channel cases. The major results are presented in chapter 6. They are explained and discussed. A short conclusion of the results and an outlook on some possible continuing investigations is given in chapter 7.

2. Fundamentals

This chapter is about the necessary fundamentals for the present thesis. First, the governing equations for incompressible flows, the Navier–Stokes equations, are presented. For many cases, these need to be solved numerically. One approach, the Reynolds-averaged Navier–Stokes equations, is presented in the subsequent section and two other approaches, the direct numerical simulation and the large eddy simulation are mentioned.
The third section introduces the channel flow and the Reynolds-averaged Navier–Stokes equations for this important case before some specific features in the duct flow are mentioned. The topic of the last section in this chapter is the investigated control technique.

2.1. Governing equations for incompressible fluid mechanics

Fluid mechanics can be considered as a branch of continuum mechanics. As long as the ratio of the mean free path of molecules and the length scale of interest is small enough that the Knudsen number is $Kn \ll 1$, the continuum assumption holds (Kundu et al., 2012). This means that the governing equations of continuum mechanics determine the quantities of interest. For incompressible flows those quantities are the three components of the velocity vector u, v, w and the pressure p as a Lagrangian multiplier to fulfil the continuity equation.
The governing equations of incompressible flows are the conservation of mass and momentum. The differential form of mass conservation, also known as continuity equation, is

$$\frac{\partial \rho}{\partial t} + \frac{\partial}{\partial x_i}(\rho u_i) = 0, \tag{2.1}$$

$$\frac{\mathrm{D}\rho}{\mathrm{D}t} + \rho \frac{\partial u_i}{\partial x_i} = 0. \tag{2.2}$$

The Einstein summation convention is used and u_i, x_i are the i-components of the instantaneous velocity field and the cartesian coordinate respectively. The indices i range from 1 to 3 in three dimensions. Time is denoted by t and ρ is the density. The material derivative

$$\frac{\mathrm{D}(\cdot)}{\mathrm{D}t} \equiv \frac{\partial(\cdot)}{\partial t} + u_i \frac{\partial(\cdot)}{\partial x_i} \tag{2.3}$$

of the density vanishes for incompressible flows and when the density is constant. The difference between incompressible and constant density is that for constant density both

partial derivatives are zero whereas for an incompressible fluid only the sum of both partial derivatives needs to vanish (Kundu et al., 2012). In this thesis the density is assumed to be constant. Thus, the continuity equation for incompressible flows reduces to

$$\frac{\partial u_i}{\partial x_i} = 0. \tag{2.4}$$

The differential form of the momentum equation, also known as Cauchy's equation of motion, is (Kundu et al., 2012)

$$\rho \frac{\mathrm{D}u_j}{\mathrm{D}t} = \rho \left(\frac{\partial u_j}{\partial t} + u_i \frac{\partial u_j}{\partial x_i} \right) = \rho f_j + \frac{\partial \sigma_{ij}}{\partial x_i}. \tag{2.5}$$

The j-component of the body force is denoted by f_j and σ_{ij} is the stress tensor. In general, the four unknown quantities u_1, u_2, u_3 and p are all dependent in space and time, for example $u_1 = u_1(x_1, x_2, x_3, t)$ as well as the body force $f_j = f_j(x_1, x_2, x_3, t)$. For brevity this dependency is omitted here. The body force could be for instance the gravitational acceleration or the Lorentz force in magnetohydrodynamics. Hereafter, the body force f_j will be omitted because the influence of gravity will be neglected for the present thesis and there are no other body forces acting on the fluid.
The constitutive equation which relates the stress tensor σ_{ij} with the four unknown quantities p, u_1, u_2, u_3 for an incompressible Newtonian fluid is given by

$$\sigma_{ij} = -p\delta_{ij} + \mu \left(\frac{\partial u_i}{\partial x_j} + \frac{\partial u_j}{\partial x_i} \right). \tag{2.6}$$

The Kronecker delta δ_{ij} is used which is zero for all combinations of i and j except for $i = j$ where it is 1. The dynamic viscosity is a material property. It is denoted by μ and assumed to be constant for the present thesis. The combination of the constitutive equation 2.6 and the momentum equation 2.5 with the use of the continuity equation 2.4 yields the Navier–Stokes equations (NSE) for an incompressible Newtonian fluid

$$\rho \left(\frac{\partial u_j}{\partial t} + u_i \frac{\partial u_j}{\partial x_i} \right) = -\frac{\partial p}{\partial x_j} + \mu \frac{\partial^2 u_j}{\partial x_i^2}. \tag{2.7}$$

Together with the continuity equation 2.4 these four partial differential equations are the governing equations for any incompressible, Newtonian fluid without body forces.

2.2. Numerical solution to the incompressible Navier–Stokes equations

Since there are only few analytical solutions to these partial differential equations (PDEs) for special cases, different numerical approaches to solve these equations exist. This section describes the Reynolds-averaged Navier–Stokes (RANS) equations which are often used to find a numerical solution by introducing closure terms. Direct numerical simulations, which do not need these closure terms, are mentioned together with their limitations. A third approach, the large eddy simulation (LES) is also briefly mentioned.

Due to the randomness of turbulent flows statistical approaches are used to describe the flow. One well-known statistical approach to the NSE are the RANS equations. The first step to derive the RANS equations is to decompose the instantaneous dependent-field variables (velocity and pressure) into a mean (U_j, P) and fluctuating part (u'_j, p'), the so-called Reynolds decomposition

$$u_j = U_j + u'_j, \tag{2.8}$$

$$p = P + p', \tag{2.9}$$

where the mean velocity could be defined as the average in time

$$U_j(x_1, x_2, x_3) = \langle u_j(x_1, x_2, x_3, t)\rangle = \lim_{T\to\infty} \frac{1}{T} \int_0^T u_j(x_1, x_2, x_3, t)\mathrm{d}t. \tag{2.10}$$

The brackets $\langle\cdot\rangle$ are used to denote the averaging operator, in this case the average in time. The same averaging is applied to the instantaneous pressure field.
Insertion of the decomposed velocity 2.8 into the continuity equation 2.4 and averaging shows that the mean velocity field and the fluctuating velocity field both have to satisfy the divergence-free condition

$$\frac{\partial U_i}{\partial x_i} = 0, \tag{2.11}$$

$$\frac{\partial u'_i}{\partial x_i} = 0. \tag{2.12}$$

Decomposition and insertion of velocity and pressure with subsequent averaging results in the RANS equations for an incompressible, Newtonian fluid

$$\rho\left(\frac{\partial U_j}{\partial t} + U_i\frac{\partial U_j}{\partial x_i}\right) = -\frac{\partial P}{\partial x_j} + \mu\frac{\partial^2 U_j}{\partial x_i^2} - \rho\frac{\partial}{\partial x_i}\langle u'_i u'_j\rangle. \tag{2.13}$$

A solution to the four PDEs 2.11 and 2.13 for the dependent-field variables U_1, U_2, U_3 and P can be found only when the unknown term $\langle u'_i u'_j\rangle$ is modelled. This term is often referred to as the Reynolds stress (sometimes including the density).
There is a huge variety of different models, some well-known ones are the mixing-length model and the k - ϵ-model which both belong to the class of turbulent-viscosity models.

Another approach that does not need any modelling is the direct numerical simulation. This approach is conceptually easier than the RANS equations combined with modelling terms because there is no additional modelling required and the NSE are solved directly instead of the RANS equations. It has to be noted that this is only possible if all relevant length scales are properly resolved. What seemed to be an "exciting prospect" about 50 years ago (Corrsin, 1961) is nowadays possible due to some major progress in algorithms and computational resources. In 1987 the first DNS of a channel flow was done by Kim

et al. (1987). Since then many flows in simple geometries were investigated by DNS and their results are often used as a reference due to their good agreement with experimental results.

The third approach, large-eddy simulation, can be considered as a mixture between RANS and DNS. For the large, energy containing scales the filtered NSE are solved directly whereas the residual scales are being modelled.

To conclude, the DNS is the most accurate of the three approaches because no modelling is involved which could introduce errors. However, this approach is much more expensive in terms of computational time. A very high resolution is needed to resolve the dissipative scales. Since the necessary resolution can be related to the Reynolds number (Re), it can be shown that DNS is only feasible for low Reynolds numbers. A definition of the Reynolds number for a channel flow will be given in section 2.3. Compared to RANS, DNS is much more time-consuming and needs much more computational resources. Thus, it is mostly used for research.
Solving the RANS equations instead is faster because the resolution does not need to be as high as for a DNS and the Reynolds stress is modelled. Careful consideration of the most suitable model for different cases is needed because the accuracy is not as good as with a DNS. Furthermore, there is no model which describes every flow scenario better than all the others. Due to its short run-time and applicability to higher Reynolds numbers, this is the standard industrial approach.
In between those two there is the LES. The filtered NSE are solved directly and the residual scales are modelled which leads to higher accuracy than RANS but not as good as DNS and higher computation time than RANS but not as much as DNS, all depending on the ratio of filtered and residual scales. This approach is also applicable to higher Reynolds numbers but still mostly used in research because industrial fluid mechanics is much more driven by time-constraints.

2.3. Channel flow

The turbulent channel flow is one of the simplest wall-bounded turbulent flows, why much numerical and experimental research has been done investigating this kind of flow. Some important definitions and theoretical results for the channel flow are given by Pope (2010, chapter 7.1) and will be summarized in this section.
A generic sketch of a duct flow is given in figure 2.1 (a). The flow is confined between an upper and a lower wall and two side walls. If the width of the duct B is large compared to its height H the flow far away from the side walls is thought to be statistically independent of the spanwise position z. The independence of spanwise position is modelled numerically by using periodic boundary conditions at the side walls to replicate the infinite width B. This is referred to as a channel flow and depicted in figure 2.1 (b). Streamwise, wall-normal and spanwise direction are x, y, z respectively. They are corresponding to x_1, x_2, x_3 in equations using index notation. The streamwise, wall normal and spanwise velocity are denoted by u, v, w or u_1, u_2, u_3 respectively. The geometry of the channel is defined by a length L and a channel height of $H = 2h$ with channel half height h. An additional parameter for the duct is its width B which is considered to be infinite for the channel.

A characteristic length scale for the channel flow is the channel half height h. As a characteristic velocity one can choose for instance the mean bulk velocity U_b which is defined as the spatially averaged mean streamwise velocity in the $y - z$ plane

$$U_b = \frac{1}{HB}\int_0^H \int_0^B U(y)\mathrm{d}z\mathrm{d}y = \frac{1}{H}\int_0^H U(y)\mathrm{d}y = \frac{1}{h}\int_0^h U(y)\mathrm{d}y. \tag{2.14}$$

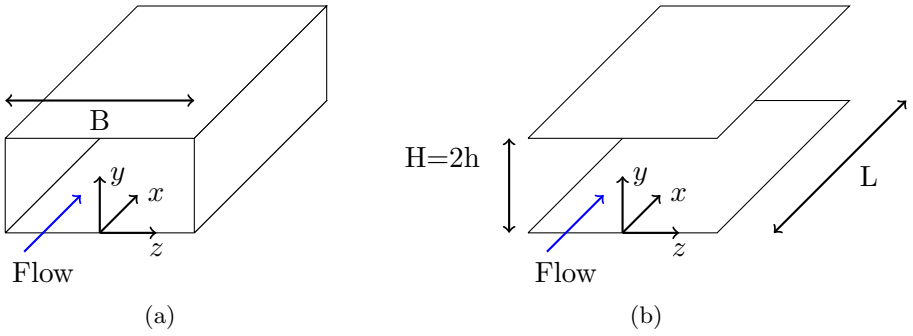

(a) (b)

Figure 2.1.: Schematic drawing of (a) duct and (b) channel flow.

In a fully developed channel flow the mean streamwise velocity only depends on wall-normal distance y and is symmetric around $y = h$.
The characteristic length scale h and velocity scale U_b can be used to define a characteristic time scale h/U_b and a characteristic pressure ρU_b^2. Those characteristic scales are used to non-dimensionalize velocity, time, cartesian coordinate and pressure:

$$u_j^* = \frac{u_j}{U_b} \quad , \quad t^* = \frac{tU_b}{h} \quad , \quad x_i^* = \frac{x_i}{h} \quad , \quad p^* = \frac{p}{\rho U_b^2}. \tag{2.15}$$

Here, the non-dimensionalized variables are denoted with the superscript *. Substitution of those non-dimensionalized quantities with those from equation 2.7 and equation 2.4 yields the non-dimensionalized NSE and continuity equation according to this non-dimensionalization

$$\frac{\partial u_j^*}{\partial t^*} + u_i^* \frac{\partial u_j^*}{\partial x_i^*} = -\frac{\partial p^*}{\partial x_j^*} + \frac{1}{Re_b} \frac{\partial^2 u_j^*}{\partial x_i^* \partial x_i^*}, \tag{2.16}$$

$$\frac{\partial u_i^*}{\partial x_i^*} = 0. \tag{2.17}$$

One of the most important dimensionless quantities for this case emerges, the bulk Reynolds number

$$Re_b \equiv \frac{hU_b}{\nu}. \tag{2.18}$$

There are several definitions for a Reynolds number in the channel flow which depend on the choice of the characteristic scales. If the mean centreline velocity $U_c = U(y = h)$ is chosen as a characteristic velocity instead of U_b the Reynolds number is defined with the centreline velocity

$$Re_c \equiv \frac{hU_c}{\nu}. \tag{2.19}$$

The Reynolds number can be interpreted as the ratio of inertial forces over viscous forces. The value of Re_b determines if the flow is either laminar $Re_b < 1350$ or turbulent $Re_b > 1800$ with transitional effects up to $Re_b = 3000$ (Pope, 2010).
The non-dimensionalized form of the NSE 2.16 and continuity equation 2.17 facilitates the transferability of different setups. As long as geometrical similarity is ensured and the dimensionless quantities such as the Reynolds number are kept constant, all non-dimensionalized flow quantities are the same (Spurk, 2010). This is essential to experiments on prototypes in wind-tunnel facilities and also on the setup of numerical experiments.
The non-dimensionalized parameters will be used for all the investigated cases in chapter 4. The following presentation of the NSE and continuity equation for the channel flow will be using dimensional quantities again, according to Pope (2010)'s notation.

The governing equations can be specialized for a channel flow. The mean continuity equation 2.11 simply yields $V = 0$ because U is independent of x in a fully developed flow, $W = 0$ and no-slip boundary conditions are assumed.
The mean momentum equation for a steady channel flow in wall-normal direction y reads

$$0 = \frac{1}{\rho}\frac{\partial P}{\partial y} + \frac{\partial}{\partial y}\langle v'v'\rangle, \tag{2.20}$$

$$0 = \frac{1}{\rho}(P - P_w) + \langle v'v'\rangle, \tag{2.21}$$

where equation 2.21 is derived by integration in wall-normal direction and $\langle v'v'\rangle|_{y=0} = 0$. P_w is the mean pressure at the wall $y = 0$ and is only dependent on streamwise position x. Thus, one can infer that

$$\frac{\partial P}{\partial x} = \frac{\mathrm{d}P_w}{\mathrm{d}x}, \tag{2.22}$$

which can be used to rewrite the streamwise momentum equation

$$0 = \nu\frac{\mathrm{d}^2U}{\mathrm{d}y^2} - \frac{\mathrm{d}}{\mathrm{d}y}\langle u'v'\rangle - \frac{1}{\rho}\frac{\partial P}{\partial x}, \tag{2.23}$$

$$0 = \frac{\mathrm{d}}{\mathrm{d}y}\left(\mu\frac{\mathrm{d}U}{\mathrm{d}y} - \rho\langle u'v'\rangle\right) - \frac{\mathrm{d}P_w}{\mathrm{d}x}. \tag{2.24}$$

The kinematic viscosity ν is defined as $\nu \equiv \mu/\rho$. The combination of viscous shear stress and turbulent shear stress can be identified as the total shear stress

$$\tau = \mu\frac{\mathrm{d}U}{\mathrm{d}y} - \rho\langle u'v'\rangle. \tag{2.25}$$

The turbulent shear stress $-\rho\langle u'v'\rangle$ is one component of the Reynolds stress tensor. Equation 2.24 has a simple solution because $\tau = \tau(y)$ is only dependent on wall-normal location y whereas $P_w = P_w(x)$ is only dependent on the streamwise location x. Thus, both derivatives need to be constant. With the definition of the wall shear stress as

$$\tau_w \equiv \tau(y = 0) \equiv \mu\left.\frac{\mathrm{d}U}{\mathrm{d}y}\right|_{y=0} \tag{2.26}$$

this constant is defined as τ_w. An often used non-dimensional parameter formed of τ_w is the skin-friction coefficient

$$C_f = \frac{2\tau_w}{\rho U_b^2}. \tag{2.27}$$

Together with the symmetry condition at $y = h$, which implies that $\tau(y = h) = 0$, a linear profile of the total shear stress is found:

$$\tau(y) = \tau_w\left(1 - \frac{y}{h}\right). \tag{2.28}$$

The previously defined wall shear stress (2.26) and the viscosity are the most important parameters close to the wall because viscous effects are dominant in this region. To come up with a different set of scaling parameters for the region close to the wall, the friction velocity or wall shear stress velocity is defined as

$$u_\tau = \sqrt{\frac{\tau_w}{\rho}}. \tag{2.29}$$

Based on the friction velocity another Reynolds number Re_τ can be defined as

$$Re_\tau \equiv \frac{u_\tau h}{\nu}. \tag{2.30}$$

The friction velocity u_τ and the kinematic viscosity ν can be used as scaling parameters close to the wall. They are referred to as viscous scales or inner scales. For the region far away from the wall, where viscous effects are negligible, there are the centreline velocity U_c or the bulk velocity U_b and channel half height h as scaling parameters. These are referred to as outer scales.

A dimensional analysis of the channel flow reveals that the six parameters which fully describe the flow (U, u_τ, ρ, ν, h, y) can be reduced to three non-dimensional quantities. Instead of using the mean streamwise velocity its wall-normal gradient is used. The result of the dimensional analysis is the relation between the three non-dimensional quantities,

$$\frac{\mathrm{d}U}{\mathrm{d}y}\frac{y}{u_\tau} = \Phi\left(\frac{yu_\tau}{\nu}, \frac{y}{h}\right), \tag{2.31}$$

where Φ is a universal non-dimensional function.
In close proximity to the wall the third non-dimensional quantity is neglected ($y/h \ll 1$). This region is called the inner layer and equation 2.31 can be simplified and scaled with the viscous scales,

$$\frac{\mathrm{d}u^+}{\mathrm{d}y^+} = \frac{1}{y^+}\Phi_1(y^+). \tag{2.32}$$

The viscous scaling of the mean streamwise velocity U and the wall-normal direction y is given by

$$u^+ = \frac{U}{u_\tau}, \tag{2.33}$$

$$y^+ = \frac{yu_\tau}{\nu}. \tag{2.34}$$

The integral yields the well known law of the wall

$$u^+ = \int_0^{y^+} \frac{1}{\bar{y}}\Phi_1(\bar{y})\mathrm{d}\bar{y}, \tag{2.35}$$

where the right-hand side is only dependent on y^+. For small values of y^+ a Taylor series expansion of the right-hand side shows that the integral can be approximated by y^+. This yields the expression for the viscous sublayer ($y^+ < 5$)

$$u^+ = y^+. \tag{2.36}$$

Still in the inner layer ($y/h < 0.1$) but for larger values of y^+, viscous effects become more and more negligible. This means that the universal non-dimensional function Φ_1 also loses its dependence on y^+ and becomes a constant κ^{-1}. This constant is the von Kármán constant. Using this fact in equation 2.32 and integrating gives the logarithmic law of the wall,

$$\frac{\mathrm{d}u^+}{\mathrm{d}y^+} = \frac{1}{\kappa y^+}, \tag{2.37}$$

$$u^+ = \frac{1}{\kappa}\ln(y^+) + C. \tag{2.38}$$

The two constants κ and C are suggested by (Pope, 2010) to take the following values:

$$\kappa = 0.41, \qquad C = 5.2. \tag{2.39}$$

2.4. Duct flow

For an infinitely wide duct the flow in the centre can be be described by the equations for the channel flow presented above. If the width is not much larger than the height the effect of the side walls is not negligible and the assumption of spanwise independence is not valid anymore.
Two features which are absent in the channel are the secondary flow and the boundary layers growing on the side walls. The latter are responsible for an increased streamwise velocity at the core of the duct when compared to a channel with the same bulk velocity. This is due to the decreased streamwise velocity in the vicinity of the side walls which in exchange leads to an increased streamwise velocity in the core region. This leads to an increase in wall shear stress at the centreplane ($z = 0$) of the duct (Vinuesa et al., 2014).
The other remarkable feature of a turbulent duct flow is the presence of the secondary flow field. According to Oertel jr. (2012) this cross-flow arises as a result of fluid being transported to the core at regions of high wall shear stress and in exchange at regions of low wall shear stress, for instance at the corners, fluid moves towards the wall. This leads to a pattern of one pair of counter rotating vortices at each corner of the rectangular duct as can be seen for instance in Gessner and Jones (1965). The formation of those vortices can be further understood by investigating the mean streamwise vorticity, Ω, transport equation for a fully developed straight duct flow (Gavrilakis, 1992),

$$\begin{aligned} &V\frac{\partial\Omega}{\partial y} + W\frac{\partial\Omega}{\partial z} - \nu\left(\frac{\partial^2}{\partial y^2} + \frac{\partial^2}{\partial z^2}\right)\Omega \\ &= -\frac{\partial^2}{\partial y \partial y}\left(\langle w'^2\rangle - \langle v'^2\rangle\right) - \left(\frac{\partial^2}{\partial y^2} - \frac{\partial^2}{\partial z^2}\right)\langle v'w'\rangle, \end{aligned} \tag{2.40}$$

where the mean streamwise vorticity is given by

$$\Omega = \frac{\partial W}{\partial y} - \frac{\partial V}{\partial z}. \tag{2.41}$$

The terms on the left-hand side of equation 2.40 are the mean flow convection and viscous diffusion of the mean streamwise vorticity. The two terms on the right-hand side contribute to the production of the mean streamwise vorticity, which is why this secondary flow is also known as Reynolds-stress-induced secondary flow (or Prandtl's second kind according to Prandtl (1926)). Therefore, this type of secondary flow only arises for turbulent flows and is consequently non-existent for a laminar flow (Gessner and Jones, 1965).

As pointed out by Vinuesa et al. (2014), the two three-dimensional effects present in the duct, *i.e.* side wall boundary layers and secondary flow, have competing effects on the flow. The boundary layer growth from the side walls increases momentum in the core region and consequently the wall shear stress at the centre of the duct is increased. In contrast, the secondary motions transport momentum from the core region towards the corner bisectors, thus, decreasing the wall shear stress in the centre.

One interesting quantity to quantify the magnitude of the secondary flow is its kinetic energy defined as

$$K := \frac{1}{2}(V^2 + W^2), \tag{2.42}$$

which will be used later to assess the differences in the secondary flow field between the uncontrolled and controlled cases.

2.5. Control technique

The aim of the applied flow control technique in this thesis is to achieve high drag reduction. Fukagata et al. (2002) show that the skin-friction coefficient for a fully developed turbulent channel flow driven at constant flow rate can be decomposed into a laminar and a turbulent contribution

$$C_f = \frac{12}{Re_b} + 12 \int_0^1 2(1-y)(-\langle u'v' \rangle) \mathrm{d}y. \tag{2.43}$$

This equation shows why the skin-friction drag of the fully developed turbulent channel is usually much larger than that of the laminar one since the second term vanishes for the latter and is usually positive. Therefore, in order to achieve turbulent drag reduction $-\langle u'v' \rangle$ is desired to decrease.

The flow control technique used for the simulations in this thesis is the harmonic oscillation of the upper and lower walls. This technique was chosen because it is simple, easy to implement and leads to high drag reduction. Drag reduction DR is defined by

$$DR := \frac{C_{f,0} - C_{f,c}}{C_{f,0}}, \tag{2.44}$$

where $C_{f,0}$ and $C_{f,c}$ denote the skin-friction coefficient of the uncontrolled reference case and the controlled case, respectively.

The harmonic oscillation of the horizontal walls is similar to Stokes' second problem. Even though the solution to Stokes' second problem is only a solution to the 2D laminar problem it agrees very well with the phase averaged spanwise velocity of controlled channel cases as is shown by Choi and Xu (2002) and Choi (2002) which is another reason why this problem is presented here.
Stokes' second problem is one of the few flows that can be described by an analytical solution to the Navier–Stokes equations for the laminar case. It is characterized by an infinite flat plate that oscillates in a harmonic motion under an initially quiescent fluid. This is depicted in figure 2.2.

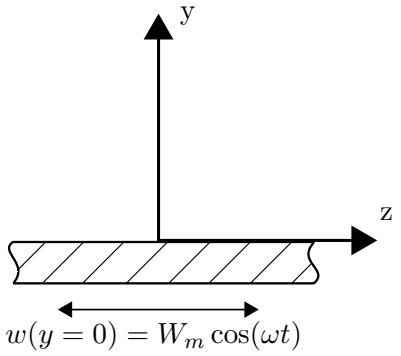

Figure 2.2.: Sketch of Stokes' second problem.

The two boundary conditions are

$$w(y=0,t) = W_m \cos(\omega t), \tag{2.45}$$

$$w(y \to \infty, t) = 0. \tag{2.46}$$

W_m is the amplitude of the wall velocity and ω is the oscillation frequency. The initial transients are not considered here, only the steady periodic solution. The Navier–Stokes

equations reduce to the momentum equation in horizontal direction,

$$\frac{\partial w}{\partial t} = \nu \frac{\partial^2 w}{\partial y^2}. \tag{2.47}$$

The solution to this partial differential equation can be found in the literature (Schlichting and Gersten, 2006). It is given as

$$w(y,t) = W_m \exp\left(-y\sqrt{\frac{\omega}{2\nu}}\right) \cos\left(\omega t - y\sqrt{\frac{\omega}{2\nu}}\right). \tag{2.48}$$

Some solutions to this problem are given in figure 2.3.

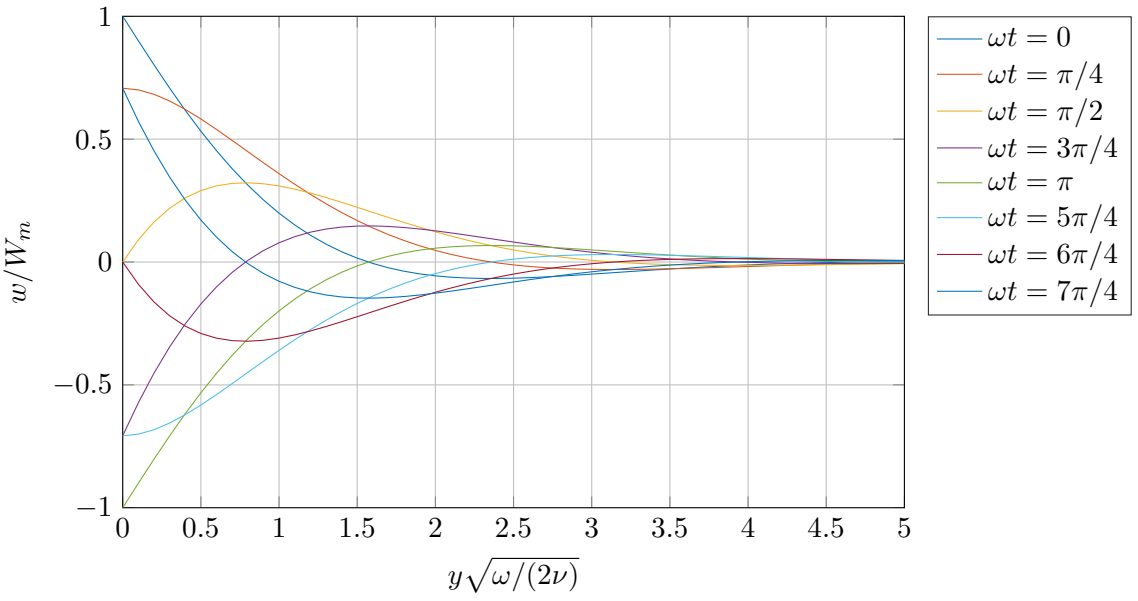

Figure 2.3.: Solutions to Stokes' second problem.

3. Numerical methods

This chapter is about the numerical methods used in the present thesis. The spectral element method will be presented by introducing the weighted residual technique, particularly the Galerkin method. Based on the weak formulation of a model problem the spatial discretization will be described. Next, the temporal discretization is shown for another model problem and the last part of this chapter deals with parallelization.

3.1. Weighted residual techniques: Galerkin method

The first to propose the spectral element method was Patera (1984). The idea was to combine the finite element method with spectral techniques in order to benefit from both the high accuracy achieved by spectral techniques and the versatility of the finite element method when it comes to complex geometries.
The basics of the spectral element method will be presented by solving a model problem, the Poisson equation in 1D,

$$-\frac{\mathrm{d}^2 u_{ex}}{\mathrm{d}x^2} = f(x), \qquad x \in [0,1], \qquad u_{ex}(0) = u_{ex}(1) = 0. \tag{3.1}$$

This can be considered as a subproblem of the NSE. Here, u_{ex} is the exact solution to the problem and the boundary conditions are of Dirichlet type and homogeneous. The first step is to choose a finite-dimensional trial space $X_0^N := span\{\phi_1(x), \phi_2(x), \phi_3(x), ..., \phi_N(x)\}$. The basis functions of this space satisfy the homogeneous boundary condition

$$\phi_j(0) = \phi_j(1) = 0, \qquad \forall j, \tag{3.2}$$

which is indicated by the subscript 0 for the trial space. The trial solution $u(x)$ can then be defined as

$$u(x) = \sum_{j=1}^{N} \phi_j(x)\hat{u}_j. \tag{3.3}$$

The basis coefficients are denoted by $\hat{u}_j$. In general, this trial solution will not solve the model problem equation 3.1 and a residual function $r(x)$ can be defined as

$$r(x) := f(x) + \frac{\mathrm{d}u(x)}{\mathrm{d}x^2}. \tag{3.4}$$

Common to all weighted residual techniques is the requirement that the integral of the weighted residual is zero. Therefore, test functions $v \in Y_0^N$ and a test space Y_0^N are needed but not further defined at this point,

$$\int_0^1 vr\mathrm{d}x = 0, \qquad \forall v \in Y_0^N. \tag{3.5}$$

This equation can be interpreted as the requirement of the residual r to be orthogonal to the test function v in terms of $\mathcal{L}^2$,

$$\mathcal{L}_\Omega^2 = \left\{ v : \int_\Omega v^2 \mathrm{d}x < \infty \right\}. \tag{3.6}$$

$\mathcal{L}^2$ denotes the space of Lebesgue-square-integrable functions and Ω denotes the whole domain of the problem.
One special type of weighted residual techniques is the Galerkin formulation. In this type the trial space X_0^N is equal to the test space Y_0^N. Using the Galerkin formulation and the definition of the residual inserted into equation 3.5 gives

$$-\int_0^1 v\frac{\mathrm{d}^2 u}{\mathrm{d}x^2}\mathrm{d}x = \int_0^1 vf\mathrm{d}x, \qquad \forall v \in X_0^N, \qquad u \in X_0^N. \tag{3.7}$$

Integration by parts is used to rewrite the left-hand side

$$-\int_0^1 v\frac{\mathrm{d}^2 u}{\mathrm{d}x}\mathrm{d}x = -\left[v\frac{\mathrm{d}u}{\mathrm{d}x}\right]_0^1 + \int_0^1 \frac{\mathrm{d}v}{\mathrm{d}x}\frac{\mathrm{d}u}{\mathrm{d}x}\mathrm{d}x = \int_0^1 (v)'(u)'\mathrm{d}x. \tag{3.8}$$

In this context the $(\cdot)'$ denotes the first derivative.
The term evaluated at the boundaries vanishes because $v \in X_0^N$ satisfies the homogeneous boundary conditions. This allows to rewrite equation 3.7 to:
Find $u \in X_0^N$ such that

$$\int_0^1 (v)'(u)'\mathrm{d}x = \int_0^1 vf\mathrm{d}x, \qquad \forall v \in X_0^N. \tag{3.9}$$

This is the so-called weak form because $u(x)$ does not need to be twice differentiable anymore as in equation 3.7. Thus, the restrictions for X_0^N are weakened and it is sufficient to require that $X_0^N \subset \mathcal{H}_0^1$. Here, $\mathcal{H}_0^1$ denotes the Sobolev space which satisfies the homogeneous boundary conditions and is defined as

$$\mathcal{H}_0^1 = \left\{ v : v \in \mathcal{L}^2, \frac{\mathrm{d}v}{\mathrm{d}x} \in \mathcal{L}^2, v|_{\partial\Omega} = 0 \right\}. \tag{3.10}$$

Here, $\partial\Omega$ denotes the boundary of the problem domain Ω. In other words, the Sobolev space $\mathcal{H}_0^1$ includes all functions which are Lebesgue-square-integrable, their first derivatives are Lebesgue-square-integrable and they satisfy the homogeneous boundary conditions. It can be shown that the trial solution $u(x)$ is the best solution among all solutions in the trial space in terms of the energy norm. This is shown in Appendix A.

The discretization of the weak formulation of the model problem 3.9 is achieved by introducing the trial solution and test function as a linear combination of basis functions according to 3.3. The same procedure is used for the discretization of the right-hand side

f for now, even though f does not need to be in X_0^N.

$$\int_0^1 (v)'(u)'\mathrm{d}x = \int_0^1 vf\mathrm{d}x \tag{3.11}$$

$$\int_0^1 \left(\sum_{j=1}^{N} \hat{v}_j(\phi_j)'\right)\left(\sum_{j=1}^{N} \hat{u}_j(\phi_j)'\right)\mathrm{d}x = \int_0^1 \left(\sum_{j=1}^{N} \hat{v}_j\phi_j\right)\left(\sum_{j=1}^{N} \hat{f}_j\phi_j\right)\mathrm{d}x \tag{3.12}$$

$$\sum_{j=1}^{N}\sum_{i=1}^{N} \hat{v}_j\left(\int_0^1 (\phi_j)'(\phi_i)'\mathrm{d}x\right)\hat{u}_i = \sum_{j=1}^{N}\sum_{i=1}^{N} \hat{v}_j\left(\int_0^1 \phi_j\phi_i\mathrm{d}x\right)\hat{f}_i \tag{3.13}$$

The definition of the stiffnes matrix A and the mass matrix B

$$A_{ij} := \int_\Omega \frac{\mathrm{d}\phi_j}{\mathrm{d}x}\frac{\mathrm{d}\phi_i}{\mathrm{d}x}\mathrm{d}x, \tag{3.14}$$

$$B_{ij} := \int_0^1 \phi_j\phi_i\mathrm{d}x \tag{3.15}$$

together with vector notation for the basis coefficients

$$\hat{u}_i := (u_1, u_2, ..., u_n)^T = \underline{u}^T, \tag{3.16}$$

$$\hat{v}_i := (v_1, v_2, ..., v_n)^T = \underline{v}^T, \tag{3.17}$$

$$\hat{f}_i := (f_1, f_2, ..., f_n)^T = \underline{f}^T \tag{3.18}$$

permit a very compact notation of the system of linear equations

$$\sum_{j=1}^{N}\sum_{i=1}^{N} \hat{v}_j A_{ij}\hat{u}_i = \sum_{j=1}^{N}\sum_{i=1}^{N} \hat{v}_j B_{ij}\hat{f}_i \tag{3.19}$$

$$\underline{v}^T A\underline{u} = \underline{v}^T B\underline{f}. \tag{3.20}$$

So far the procedure is common to all Galerkin methods. The difference between the SEM and other Galerkin methods stems only from the choice of an appropriate trial space and its associated basis functions. One difference between the SEM/FEM and fully spectral techniques is the use of basis functions that have local support only in the SEM/FEM whereas for fully spectral techniques global bases are used. Global bases extend over the entire domain. Local bases are different in that the individual basis functions vanish on the whole domain except at one specific element. This so-called local support of the basis functions allows a discretization of the geometry with a flexible distribution of grid points. Hence, a discretization of more complex geometries becomes feasible.
The difference between FEM and SEM arises from the fact that orthogonality between basis functions is ensured only by the local nature of the basis functions for FEM. In contrast, in the SEM orthogonality is not only due to the use of local bases but also due to the choice of orthogonal polynomials (Deville et al., 2002). An appropriate choice of orthogonal polynomials ensures a higher rate of convergence than possible with the FEM. The convergence of the FEM is algebraically which means that the error decrease by refining the mesh is limited by the polynomial order used for the basis functions (Fish and Belytschko, 2007).
For the approximation of smooth functions spectral convergence can be achieved by choosing solutions to the singular Sturm-Liouville eigenvalue problem. This means that the rate of convergence is faster than algebraically and is only governed by the smoothness of the solution (Gottlieb and Orszag, 1977).

3.2. Spatial discretization

For the SEM the trial space X_0^N is chosen to be the space of piecewise polynomials $\mathbb{P}_N$ of order N on each element Ω^e where the total number of elements is given by E and

$$\Omega = \cup_{e=1}^{E} \Omega^e \tag{3.21}$$

Legendre polynomials are chosen for the basis functions. They are a special case of Jacobi polynomials which are the only polynomial eigensolutions to the singular Sturm-Liouville problem (Deville et al., 2002). For the nodal basis Lagrangian interpolation of the Gauss–Lobatto–Legendre (GLL) quadrature nodes is used. The GLL quadrature nodes are defined on a reference element $\hat{\Omega} := \{\xi : -1 \leq \xi \leq 1\}$ by the zeros of the first derivative of the Legendre Polynomial $L'_N(\xi)$ and including the boundaries of the reference element at $\xi = -1$ and $\xi = 1$,

$$(1 - \xi^2) L'_N(\xi) = 0, \qquad \forall \xi \in \hat{\Omega}. \tag{3.22}$$

Here, ξ denotes the coordinate on the reference element.
The affine transformations between the spatial coordinate x and its respective coordinate on the reference element ξ are given by

$$\xi = \frac{2x - (x_{e-1} + x_e)}{x_e - x_{e-1}}, \qquad 1 \leq e \leq E \tag{3.23}$$

$$x = \frac{1 - \xi}{2} x_{e-1} + \frac{1 + \xi}{2} x_e, \qquad 1 \leq e \leq E. \tag{3.24}$$

The basis functions $\phi_j(x)$ can then be defined on the reference element $\hat{\Omega}$ and mapped to each element Ω^e. They are defined as Lagrangian interpolants of degree N (Deville et al., 2002)

$$\phi_j(\xi) = \frac{-1}{N(N+1)} \frac{(1 - \xi^2) L'_N(\xi)}{(\xi - \xi_j) L_N(\xi_j)}, \qquad 0 \leq j \leq N, \qquad \xi \in \hat{\Omega} \tag{3.25}$$

so they satisfy the bi-orthonormality condition

$$\phi_j(\xi_i) = \delta_{ij}. \tag{3.26}$$

The formula for the basis functions given in equation 3.25 is derived in Appendix B.

The Lagrangian interpolants for the basis functions of polynomial order $N = 5$ are shown in figure 3.1. Since the basis functions are defined by equation 3.25 and the trial space is chosen to be the space of piecewise polynomials $\mathbb{P}_N$ of order N the weak form of the model problem 3.9 can now be discretized for each element. The trial solution on a reference element is given by

$$u|_{\hat{\Omega}} = u(\xi) = \sum_{j=0}^{N} \phi_j(\xi) u_j^e, \tag{3.27}$$

where u_j^e are the basis coefficients and also the nodal values of the GLL points because

$$u(\xi_i) = \sum_{j=0}^{N} \phi_j(\xi_i) u_j^e = \sum_{j=0}^{N} \delta_{ij} u_j^e = u_i^e. \tag{3.28}$$

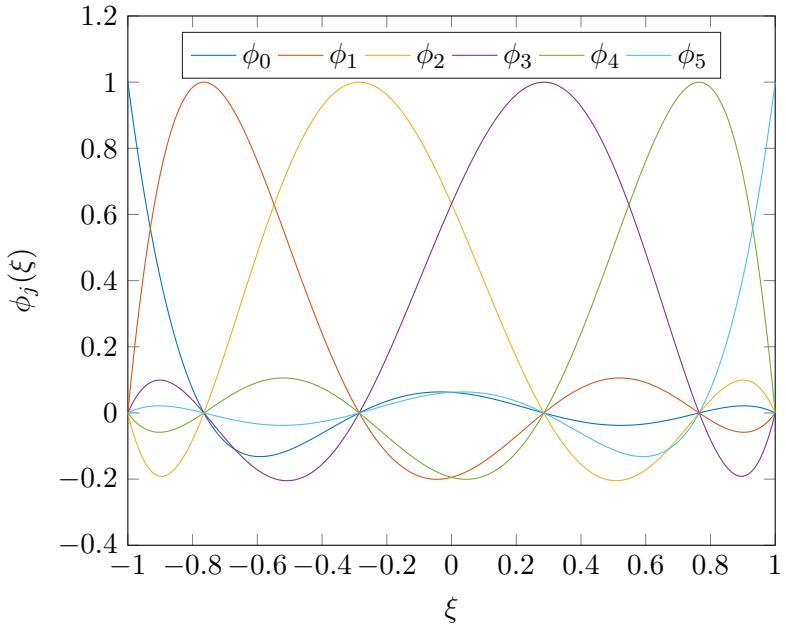

Figure 3.1.: Example of Lagrange interpolants for the Legendre spectral element basis functions on the reference element corresponding to $N = 5$.

The left-hand side of the weak form 3.9 can be written as

$$\int_\Omega (v)'(u)'\mathrm{d}x = \sum_{e=1}^{E} \int_{\Omega^e} (v^e)'(u^e)'\mathrm{d}x \tag{3.29}$$

$$= \sum_{e=1}^{E} \frac{2}{L^e} \int_{\hat{\Omega}} \frac{\mathrm{d}v(\xi)}{\mathrm{d}\xi} \frac{\mathrm{d}u(\xi)}{\mathrm{d}\xi} \mathrm{d}\xi \tag{3.30}$$

$$= \sum_{e=1}^{E} \frac{2}{L^e} \int_{\hat{\Omega}} \left(\sum_{i=0}^{N} v_i^e \frac{\mathrm{d}\phi_i(\xi)}{\mathrm{d}\xi} \right) \left(\sum_{j=0}^{N} u_j^e \frac{\mathrm{d}\phi_j(\xi)}{\mathrm{d}\xi} \right) \mathrm{d}\xi \tag{3.31}$$

$$= \sum_{e=1}^{E} \sum_{i=0}^{N} \sum_{j=0}^{N} v_i^e \left(\frac{2}{L^e} \int_{\hat{\Omega}} \frac{\mathrm{d}\phi_i(\xi)}{\mathrm{d}\xi} \frac{\mathrm{d}\phi_j(\xi)}{\mathrm{d}\xi} \mathrm{d}\xi \right) u_j^e \tag{3.32}$$

$$= \sum_{e=1}^{E} \sum_{i=0}^{N} \sum_{j=0}^{N} v_i^e A_{ij}^e u_j^e, \tag{3.33}$$

where the factor $2/L^e$ arises from the mapping onto the reference element and the element stiffness matrix A^e is given by

$$A_{ij}^e := \frac{2}{L^e} \int_{\hat{\Omega}} \frac{\mathrm{d}\phi_i(\xi)}{\mathrm{d}\xi} \frac{\mathrm{d}\phi_j(\xi)}{\mathrm{d}\xi} \mathrm{d}\xi. \tag{3.34}$$

Assembling all the nodal values in

$$\underline{u}_L := (\underline{u}^1, \underline{u}^2, ..., \underline{u}^E)^T = (u_0^1, u_1^1, u_2^1, ..., u_N^1, u_0^2, u_1^2, u_2^2, ..., u_N^2, ...u_N^E)^T, \tag{3.35}$$

$$\underline{v}_L := (\underline{v}^1, \underline{v}^2, ..., \underline{v}^E)^T = (v_0^1, v_1^1, v_2^1, ..., v_N^1, v_0^2, v_1^2, v_2^2, ..., v_N^2, ...v_N^E)^T \tag{3.36}$$

and A_L as a block-diagonal matrix accordingly, yields a compact matrix vector notation for the left-hand side of the weak form

$$\int_\Omega (v)'(u)'\mathrm{d}x = \underline{v}_L^T A_L \underline{u}_L^T. \tag{3.37}$$

For continuity every last point of each element has to have the same value as the first point of the following element, that is $u_N^e \equiv u_0^{e+1}$. Additionally, the homogeneous boundary conditions need to be taken into account. This can be achieved by two additional matrices Q and R^T which ensure that $u, v \in \mathcal{H}^1$ and $u, v \in \mathcal{H}_0^1$ accordingly. Thus, the left-hand side of the weak form can be expressed with global numbering for the inner nodes $\underline{u}$ and $\underline{v}$ as

$$\underline{v}^T R Q^T A_L Q R^T \underline{u} = \underline{v}^T A \underline{u}. \tag{3.38}$$

The right-hand side of the weak form 3.9 can be treated similarly with the definition of the element mass matrix as

$$B_{ij}^e := \frac{L^e}{2} \int_{\hat{\Omega}} \phi_i(\xi)\phi_j(\xi) \mathrm{d}\xi. \tag{3.39}$$

B_L is assembled accordingly. Not requiring continuity for $\underline{f} \in \mathcal{L}^2$ results in the right-hand side as

$$\int_0^1 v f \mathrm{d}x = \underline{v}^T R Q^T B_L \underline{f}_L = \underline{v}^T \underline{g}. \tag{3.40}$$

Therefore, the linear system of equations that needs to be solved is

$$\underline{v}^T R Q^T A_L Q R^T \underline{u} = \underline{v}^T R Q^T B_L \underline{f}_L \tag{3.41}$$

$$\underline{v}^T A \underline{u} = \underline{v}^T \underline{g} \tag{3.42}$$

$$A \underline{u} = \underline{g}. \tag{3.43}$$

Another aspect which has not been discussed yet is the evaluation of the integrals for the mass matrix and stiffness matrix. For numerical integration the integrals need to be approximated by a weighted sum. For Gauss–Lobatto integration and functions with polynomial order $\mathbb{P} \leq 2N - 1$ this approximation becomes exact. Thus, the element stiffness matrix A^e can be computed as

$$A_{ij}^e = \frac{2}{L^e} \int_{\hat{\Omega}} \frac{\mathrm{d}\phi_i(\xi)}{\mathrm{d}\xi} \frac{\mathrm{d}\phi_j(\xi)}{\mathrm{d}\xi} \mathrm{d}\xi \tag{3.44}$$

$$= \frac{2}{L^e} \sum_{k=0}^{N} \rho_k \frac{\mathrm{d}\phi_i(\xi_k)}{\mathrm{d}\xi} \frac{\mathrm{d}\phi_j(\xi_k)}{\mathrm{d}\xi} \tag{3.45}$$

$$= \frac{2}{L^e} \sum_{k=0}^{N} \rho_k D_{N,ki}^{(1)} D_{N,kj}^{(1)} \tag{3.46}$$

because the integrand is of order $2N - 2$. The differentiation matrix $D_N^{(1)}$ is defined by

$$D_{N,ij}^{(1)} := \left. \frac{\mathrm{d}\phi_j(\xi)}{\mathrm{d}\xi} \right|_{\xi=\xi_i} = \begin{cases} \dfrac{L_N(\xi_i)}{L_N(\xi_j)} \dfrac{1}{\xi_i - \xi_j}, & i \neq j, \\ -\dfrac{(N+1)N}{4}, & i = j = 0, \\ \dfrac{(N+1)N}{4}, & i = j = N, \\ 0 & \text{otherwise.} \end{cases} \tag{3.47}$$

The numerical quadrature of the mass matrix is not exact because the integrand is of the order $2N$

$$B_{ij}^e = \frac{L^e}{2}\int_{\hat{\Omega}} \phi_i(\xi)\phi_j(\xi)\mathrm{d}\xi \tag{3.48}$$

$$\approx \frac{L^e}{2}\sum_{k=0}^{N} \rho_k \phi_i(\xi_k)\phi_j(\xi_k) \tag{3.49}$$

$$= \frac{L^e}{2}\sum_{k=0}^{N} \rho_k \delta_{ik}\delta_{jk} = \frac{L^e}{2}\rho_i\delta_{ji}. \tag{3.50}$$

From this form it can be seen that the mass matrix is diagonal.
For convection dominated flows, instabilities can occur which are caused by quadrature errors. As pointed out by Malm et al. (2013) over-integration which is equivalent to dealiasing on non-uniform grids can be used to avoid this problem.

3.3. Temporal discretization

The temporal discretization which has been used for this thesis will be presented for another model problem: the unsteady convection diffusion equation,

$$\frac{\partial u}{\partial t} + c\frac{\partial u}{\partial x} = \frac{\partial}{\partial x}\left(\nu\frac{\partial u}{\partial x}\right), \tag{3.51}$$

where the convection velocity is denoted by c. The kinematic viscosity ν is assumed to be constant.
The Galerkin method and appropriate choices of basis functions and trial space as described in the previous sections result in a spatially discretized linear system of equations

$$B\frac{\mathrm{d}\underline{u}}{\mathrm{d}t} = -\nu A\underline{u} - C\underline{u}, \tag{3.52}$$

where the local spectral element convection matrix C_{ij}^e is given by

$$C_{ij}^e := \int_{\hat{\Omega}} c\phi_i \frac{\mathrm{d}\phi_j(\xi)}{\mathrm{d}\xi}\mathrm{d}\xi \qquad , 1 \le i,j \le N. \tag{3.53}$$

The diffusion term should be treated implicitly because an explicit treatment would require a very small time step to ensure stability (Deville et al., 2002). Thus, an implicit scheme is used for the temporal discretization. Application of the third order backward differencing scheme (BDF3) yields (Couzy, 1995)

$$\frac{B(11\underline{u}^{n+1} - 18\underline{u}^n + 9\underline{u}^{n-1} - 2\underline{u}^{n-2})}{6\Delta t} = -\nu A\underline{u}^{n+1} - C\underline{u}^{n+1}. \tag{3.54}$$

The short notation for $\underline{u}(t = t^n) = \underline{u}^n$ is used.
Even though the diffusion term requires an implicit treatment the convective term should rather be treated explicitly. This is because this non-symmetric term (non-linear for the NSE) is difficult to solve implicitly. The explicit scheme for the convective term which was used in this thesis is the third order extrapolation (EXT3) scheme. Application of this scheme for the convective term gives (Couzy, 1995)

$$C\underline{u}^{n+1} = 3C\underline{u}^n - 3C\underline{u}^{n-1} + C\underline{u}^{n-2} + \mathcal{O}(\Delta t)^3. \tag{3.55}$$

Substitution of this expression into 3.54 and combining all terms acting on $\underline{u}^{n+1}$ on the left-hand side and all other terms on the right-hand side results in

$$H\underline{u}^{n+1} = \underline{f}^n. \tag{3.56}$$

Here, the discrete Helmholtz operator H is defined as

$$H := \frac{11}{6}B + \Delta t \nu A \tag{3.57}$$

and the combination of terms on the right-hand side $\underline{f}^n$ is

$$\underline{f}^n := B\left(3\underline{u}^n - \frac{3}{2}\underline{u}^{n-1} + \frac{1}{3}\underline{u}^{n-2}\right) - \Delta t C\left(3\underline{u}^n - 3\underline{u}^{n-1} + \underline{u}^{n-2}\right). \tag{3.58}$$

The system of equations 3.56 needs to be solved at each timestep.

3.4. Parallelization

As described in section 2.1 a DNS is always expensive since there is no modelling involved. This means that the computational time to run the simulation is much higher than compared to a RANS. This difficulty can be overcome, at least partially, by using parallelization. For instance, the calculations for the present thesis were run in parallel on up to 528 CPUs with the spectral element code Nek5000 (Fischer et al., 2008). For its high scalability Nek5000 was awarded with the Gordon Bell prize in 1999.

4. Investigated cases

This chapter describes all the different investigated cases of this thesis. The geometrical dimensions, resolution, prescribed Reynolds number, initial flow field and boundary conditions are presented and compared. For the controlled cases the control parameters are stated. Schematic drawings of the geometry for the channel and the duct can be reviewed in figure 2.1.
For the channel flow three cases were investigated: one reference case and two controlled cases. Four different cases were investigated for the duct flow: one reference case and three controlled cases.

4.1. Channel cases

The first objective was to validate the implementation of the uncontrolled channel flow. Therefore, the first setup is adapted from Kim et al. (1987). The streamwise, wall-normal and spanwise lengths are $4\pi h$, $2h$, $2\pi h$, respectively and the bulk Reynolds number is $Re_b = 2800$. The grid points in Kim et al. (1987) were 192, 129 and 160 in streamwise, wall-normal and spanwise direction, respectively. This lead to a streamwise resolution of $\Delta x^+ = 12$ and a spanwise resolution of $\Delta z^+ = 7$. The spacing in wall-normal direction was non-uniform with the smallest spacing next to the wall at $\Delta y^+ = 0.05$ and the largest at the centreline $\Delta y^+ = 4.4$.
The geometrical dimensions were kept the same as Kim et al. (1987)'s but a different mesh was used. The mesh for this thesis was generated with 32 uniformly spaced elements in streamwise direction, 16 non-uniformly spaced elements in wall-normal direction and 32 uniformly spaced elements in spanwise direction. The polynomial order was set to 7 which gives 8 grid points per element. This lead to a grid resolution of $\Delta x^+_{max} = 14.8$, $\Delta y^+_{min} = 0.2$, $\Delta y^+_{max} = 7.3$, $\Delta z^+_{max} = 7.4$ in streamwise, wall-normal and spanwise direction respectively. The tenth point in wall-normal direction is at $y^+ = 7.5$. Note that, although the elements are spaced uniformly in the homogeneous directions the grid points within each element are not equally spaced.
According to Coleman and Sandberg (2010) the resolution requirements for a fully resolved wall-bounded flow are $\Delta x^+ < 15$ and $\Delta z^+ < 8$ for the homogeneous streamwise and spanwise directions. The resolution requirements in wall-normal direction are that the first point away from the wall should be $y^+ < 1$ and the first ten points within $y^+ < 10$. The bulk Reynolds number was kept at $Re_b = 2800$, the same level as the simulation by Kim et al. (1987).

The boundary conditions for the two channel cases are the no-slip condition at the top and bottom wall and periodic boundary conditions at the side walls and at the inlet and outlet. The state of fully developed turbulence was reached by a laminar flow as an initial field submitted to disturbances. These disturbances were introduced by a numerical "tripping" as described in Schlatter and Örlü (2012). The numerical "tripping" is generating a weak random volume force in the wall normal direction causing the laminar flow to become unstable and turbulent. The "tripping" was used for the first 50 time units on a coarser mesh where the polynomial order was set to 5. Note that the non-dimensionalization of the time was done with h and U_b as shown in section 2.3 and is used if nothing else is mentioned. For the next 50 time units the polynomial order was set to 7 and the "tripping" was turned off so that the turbulent flow could develop without any artificial forces. The collection of data for later post-processing was done from $t = 100$ to $t = 400$ time units. The pressure gradient was used as the criteria to decide when to start collecting data for post-processing for this case and all other cases in this thesis. Visual inspection of its development showed that the initial transients had died out until $t = 100$. This first reference channel flow is denoted by c:0 where c abbreviates channel and 0 stands for zero wall velocity.

The second case which was investigated is a controlled channel flow. The geometrical dimensions, the mesh, and the bulk Reynolds number are kept at the same values as for the uncontrolled channel flow. The only difference is the boundary condition at the wall as depicted in figure 4.1. The movement of the wall is illustrated by the green color and the arrows. Both the upper and lower wall are moving in spanwise direction with a prescribed

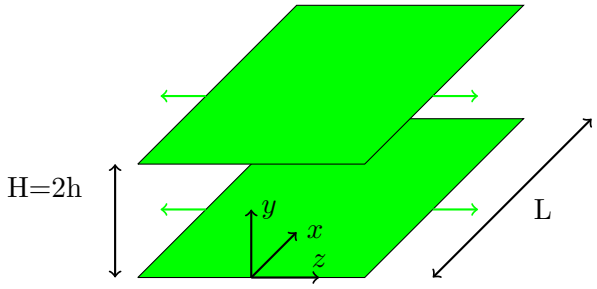

Figure 4.1.: Schematic drawing of controlled channel flow.

velocity. The spanwise velocity of the fluid at the wall $y = 2h$ or $y = 0$ is given by the harmonic oscillation of the wall

$$w(y = 0) = w(y = 2h) = W_m \sin\left(\frac{2\pi}{T}t\right). \tag{4.1}$$

The two parameters for the harmonic wall oscillation are the amplitude of the wall velocity W_m and the time period T. Those parameters were set to $W_m^+ = 12$ and $T^+ = 125$. This case is denoted by c:12 where 12 stands for the amplitude of the wall velocity set for this case. Note that the conversion in plus units is done with the averaged uncontrolled friction velocity $u_{\tau,0}$ which was extracted from the uncontrolled case. For all the simulations the flow rate was kept constant. This means that the friction velocity will be different for the reference case and the controlled cases.
Those parameters were chosen because according to Quadrio and Ricco (2004) the optimum time period is $T^+ = 125$ and for $W_m^+ = 12$ significant effects could be expected. A higher value for W_m^+ would have increased the effects of control even more. However, this value was also used for one of the controlled duct cases. A higher value of W_m^+ for the controlled duct case increases the run-time because the time step needs to be decreased. This is due to the fact that the elements close to the side walls are necessarily very small but the spanwise velocity is relatively high due to the boundary condition. So this value

for the amplitude of wall velocity was a trade-off between large drag reduction and small run-time for the duct cases. The boundary conditions in the homogeneous directions are periodic as for the reference case. The movement of the top and bottom wall is implemented as a prescribed velocity directly at those walls. The initial flow field was taken from the turbulent flow field of the uncontrolled reference case after 300 time units. Data was collected from $t = 508$ to $t = 808$.

A second controlled channel case was set up exactly the same as the first controlled channel case but with a smaller $W_m^+ = 4.5$ for comparison with the corresponding controlled duct case. Using the same notation as for the other channel cases, this case is denoted by c:4.5.

4.2. Duct cases

The reference duct case, denoted by d:0, has slightly different geometrical parameters than the previously described channel cases. The streamwise, wall-normal and spanwise lengths are $12.5h$, $2h$ and $6h$, respectively. Additionally, the bulk Reynolds number was reduced to $Re_b = 2581$. There are two reasons for this change. First, results for this setup of the duct flow were generated in the past and made available for this thesis (Vinuesa et al., 2014). They were conducted with a higher resolution and were used as a comparison for the present results. Second, for a comparison between duct flow and channel flow a constant bulk Reynolds number in the centre plane $Re_{b,c}$ defined with the bulk velocity at the centre plane $U_{b,c}$ is more important than keeping Re_b at the same level as before. At least in the centre plane the bulk Reynolds number is then kept at the same value. The decrease of the bulk Reynolds number Re_b was done in such a way to keep $Re_{b,c}$ almost at the same level for the duct and the channel.
The number of elements in streamwise direction was kept at 32 and they were again uniformly spaced. The distribution of elements in wall-normal direction was also kept the same as for the channel flow: 16 non-uniformly spaced. However, in spanwise direction the elements cannot be distributed uniformly anymore because of the effects of the side walls. The guidelines by Coleman and Sandberg (2010) mentioned above were used to design the spanwise distribution of elements in order to satisfy the requirements for a fully resolved DNS. Therefore, 36 not uniformly spaced elements were used in spanwise direction. The maximum distance between two grid points was $\Delta x^+_{max} = 14.7$, $\Delta y^+_{max} = 7.3$ and $\Delta z^+_{max} = 7.5$ in streamwise, wall-normal and spanwise direction respectively. The first point away from the wall was at $y^+ = 0.4$ and $z^+ = 0.4$ respectively and the tenth point away from the wall was at $y^+ = 9.9$ and $z^+ = 9.9$. The resolution close to the side walls was a crucial factor which determined the maximum time step for one of the controlled duct cases. This is because of the large spanwise velocity close to the side walls induced by the moving walls for the controlled cases. Again, the geometrical dimensions, the mesh and the bulk Reynolds number were kept constant for all the different duct cases. A summary of all the geometrical parameters, the resolution and the Reynolds number of the reference channel and duct cases can be found in table 4.1.
The boundary conditions for the uncontrolled duct case are the no-slip condition with zero velocity at the top and bottom walls as well as at the side walls. Periodic boundary conditions are applied to the inlet and outlet. A laminar duct flow expansion as described in Panton (2013, chapter 11.2) was used as the initial flow field. Again, the numerical "tripping" was used to generate a turbulent flow. For the reference duct case this "tripping" was turned on only during the first 15 time units (where the non-dimensionalization was done using U_b and h as shown in section 2.3) and turned off afterwards. The collection of data was done from $t = 200$ to $t = 3000$. The time for collecting samples needs to be longer than in the channel cases because averaging in spanwise direction is not possible anymore.

Table 4.1.: Comparison of geometrical parameters, resolution and Reynolds number between channel and duct reference cases.

	c:0	d:0
Length	$4\pi h$	$12.5h$
Width	$2\pi h$	$6h$
Height	$2h$	$2h$
Aspect ratio	π	3
Number of elements in x	32	32
Number of elements in y	16	16
Number of elements in z	32	36
Polynomial order	7	7
Δx^+_{max}	14.8	14.7
Δy^+_{max}	7.3	7.3
Δy^+_{min}	0.2	0.4
y^+_{10}	7.5	9.9
Δz^+_{max}	7.4	7.5
Δz^+_{min}	2.3	0.4
z^+_{10}	/	9.9
Re_b	2800	2581

The controlled and the reference duct cases only differ in the boundary conditions and the initial condition. The initial flow field for all of the controlled duct cases is the uncontrolled duct case after 1000 time units. Data for the controlled duct cases was collected from $t \approx 1200$ until $t \approx 3000$ for all three controlled duct cases.
The region of wall movement is different for the third control case. Figure 4.2 shows the moving area of the walls in green and the static area of the walls in white for the three controlled duct cases. A movement of almost the whole upper and lower wall was applied

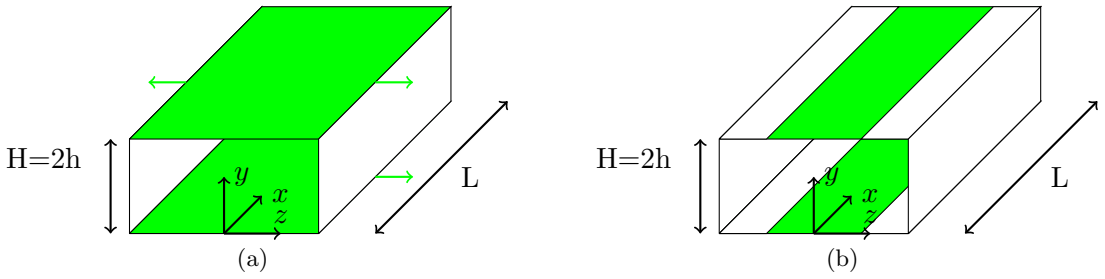

Figure 4.2.: Schematic drawing of (a) controlled duct cases 1 and 2 and (b) case 3.

for the controlled cases 1 and 2. If the whole upper and lower wall were moving this could cause numerical problems. For instance, the corner edge belongs to both the side walls and the upper or lower wall. Therefore, two velocities would be prescribed at this edge. A test run for a lid-driven cavity case showed that these problems could be avoided by increasing the velocity from zero at the edges in a short region smoothly to the prescribed value. Therefore, a smoothed "step" function of the following form was implemented

$$S(x) = \begin{cases} 0, & x \leq 0, \\ \dfrac{1}{1+\exp\left(1/(x-1)+1/x\right)}, & 0 < x < 1, \\ 1, & x \geq 1. \end{cases} \tag{4.2}$$

It was adjusted so that it rises close to the corner at $z = -3$ and falls in the same way at $z = 3$. The adjusted smoothed "step" function applied to the controlled duct cases 1 and 2 is given by

$$\lambda(z) = S\left(\frac{z+3}{\Delta\lambda}\right) \cdot S\left(\frac{-z+3}{\Delta\lambda}\right), \tag{4.3}$$

where $z + 3$ does the shift and the factor $\Delta\lambda = 0.035$ determines the width of the rise and fall. The region close to $z = -3$ is depicted in figure 4.3. This function 4.3 is then

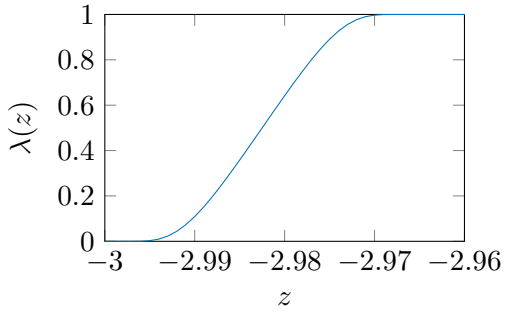

Figure 4.3.: The smoothed step function applied to a region close to $z = -3$.

multiplied by the amplitude of wall velocity W_m to set the boundary conditions at the moving walls of the duct cases.
Cases 1 and 2 only differ in the control parameters. Case 1 uses $W_m^+ = 4.5$ and case 2 uses $W_m^+ = 12$ for the amplitude of the wall velocity. They are denoted by d:4.5 and d:12, respectively. The time period is again set to the optimum value of $T^+ = 125$ as it was set for the controlled channel flow. The third control case applies the wall movement only to the inner part of the upper and lower wall as shown in Figure 4.2b. More precisely, it is applied the region between $z = -1.5$ and $z = 1.5$ again using the previously described smoothed "step" function with the same width of rise and fall $\Delta\lambda = 0.035$. The lower amplitude of wall velocity was chosen for this case due to the physical impracticabilty of a too large wall displacement confined only to this part of the wall. This case is denoted by p:4.5 where p abbreviates partial. A comparison of the control parameters for all the investigated control flows is given in table 4.2.

Table 4.2.: Different control parameters for channel and duct cases.

	c:12	c:4.5	d:4.5	d:12	p:4.5
W_m^+	12	4.5	4.5	12	4.5
T^+	125	125	125	125	125
moving region	$[-3, 3]$	$[-3, 3]$	$[-3, 3]$	$[-3, 3]$	$[-1.5, 1.5]$

5. Validation

This chapter deals with the validation of the implementation of the uncontrolled and controlled channel cases. In order to ensure that the implementation for those and the succeeding duct cases is correct the generated results are compared to data from the literature and to data generated with a classical pseudo-spectral code. The setup of the channel cases is described in chapter 4.1.

5.1. Uncontrolled channel flow

The first objective was to recreate the results from the DNS by Kim et al. (1987) of the uncontrolled channel flow at $Re_\tau = 180$. Therefore, a simulation set up in Nek5000 was compared to their results. In order to not get any effects from the transient at the beginning and to collect enough independent samples the statistical quantities of interest were collected between $t = 100$ and $t = 400$ time units. As previously, h and U_b were used for non-dimensionalization if nothing else is mentioned.
Good qualitative agreement between their results and the results of the present thesis was found. However, their complete data was not available. Therefore, some of the mean flow variables given in their article are compared to the present results in table 5.1. Table 5.1 shows the good agreement for the mean flow variables. Additionally, a comparison of the plots showed generally good agreement.

Table 5.1.: Comparison of some mean flow variables between the present thesis and the results from Kim et al. (1987).

	c:0	Kim et al. (1987)
Re_b	2800	≈ 2800
Re_τ	179.3	≈ 180
Re_c	3266	≈ 3300
U_c/U_b	1.16	1.16
C_f	$8.20 \cdot 10^{-3}$	$8.18 \cdot 10^{-3}$

A more detailed comparison of the results generated by Nek5000 with literature data was conducted with the DNS data of Moser et al. (1999) as their data was available. They chose a slightly different geometry of $4\pi h$, $2h$ and $4/3\pi h$ for the streamwise, wall-normal and spanwise length respectively. Their resolution for the case with $Re_\tau = 180$ was $\Delta x^+ = 17.7$, $\Delta y^+_{center} = 4.4$ and $\Delta z^+ = 5.9$ in streamwise, wall-normal and spanwise

direction respectively. Their data is denoted by MKM in the following plots. A second set of data was generated with a classical pseudo-spectral code for the uncontrolled channel flow with $Re_\tau = 180$. This code is described in Luchini and Quadrio (2006) and denoted by CPL as it is written in the programming language CPL.
Figure 5.1 shows the dependency of the mean streamwise velocity u^+ (a) and the Reynolds stress $\langle u'v' \rangle^+$ (b) on the wall-normal direction y^+.

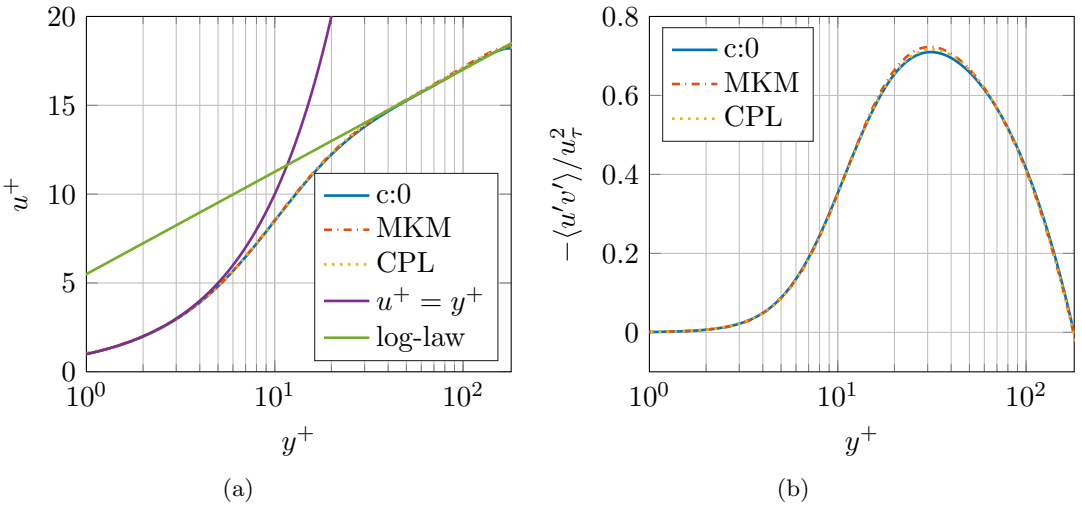

Figure 5.1.: Mean streamwise velocity u^+ (a) and Reynolds stress $\langle u'v' \rangle / u_\tau^2$ (b) in the uncontrolled channel.

The wall-normal distance y^+ uses a logarithmic axis and only goes to the channel half height h because of a symmetrical behaviour in the upper half of the channel. This symmetry was used appropriately to improve the statistics. The logarithmic law of the wall given by Zierep and Bühler (2013): $u^+ = 2.5 \ln(y^+) + 5.5$ is employed. Besides, the linear relation in the viscous sublayer as derived in section 2.3 is used. For the mean streamwise velocity all three datasets coincide on one curve so they are not distinguishable. The agreement of the Reynolds stress is also good except for a slightly too low peak value for the results generated with Nek5000.

A comparison of the root-mean-square values of the turbulent fluctuating velocities u^+_{rms}, v^+_{rms} and w^+_{rms} is shown in figure 5.2. Again, the agreement between the current results and

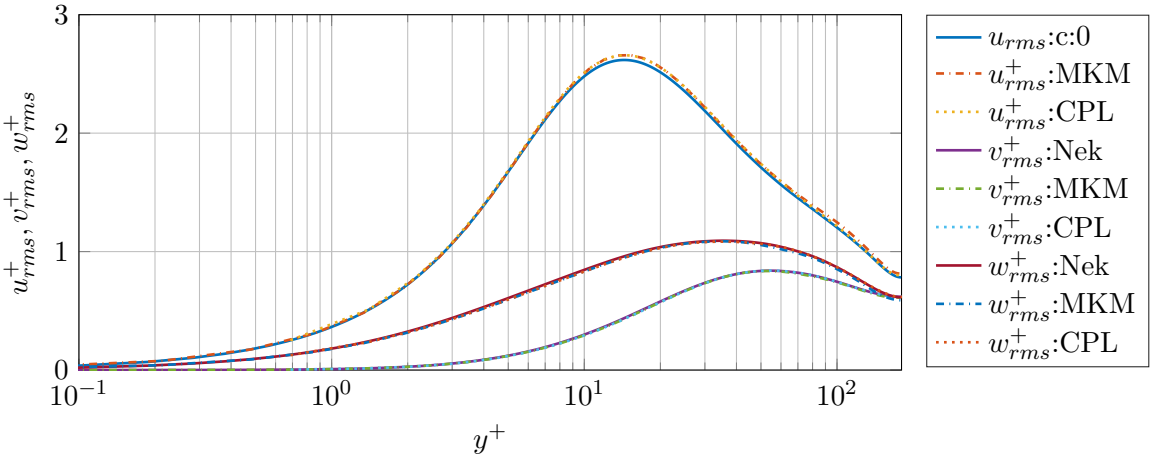

Figure 5.2.: RMS values in the uncontrolled channel.

MKM and CPL is generally good except for a slight undershoot of u_{rms}. Apart from that the curves coincide again. This undershoot might be caused by insufficient spatial resolution as pointed out by Örlü and Schlatter (2013) even though the resolution requirements by Coleman and Sandberg (2010) were satisfied. These requirements are only guidelines and meant for fully spectral methods with evenly spaced quadrature points (Coleman and Sandberg, 2010). However, the quadrature nodes of the grid for the simulation with SEM are not evenly spaced.

5.2. Controlled channel flow

For the validation of the controlled channel flow the current results were compared to the results generated with the CPL code. The collection of samples for the statistics was done between $t = 500$ and $t = 800$ time units where the control technique was applied from $t = 300$ on.
Figure 5.3 shows the mean streamwise velocity u^+ (a) and the Reynolds stress $\langle u'v' \rangle / u_\tau^2$ (b) again but this time for the controlled channel flow. The control parameters are described in section 4.1. Additionally, the results of the uncontrolled reference case, denoted by c:0, were plotted as a reference. The agreement between both results for the controlled cases is very good. The curves almost coincide.

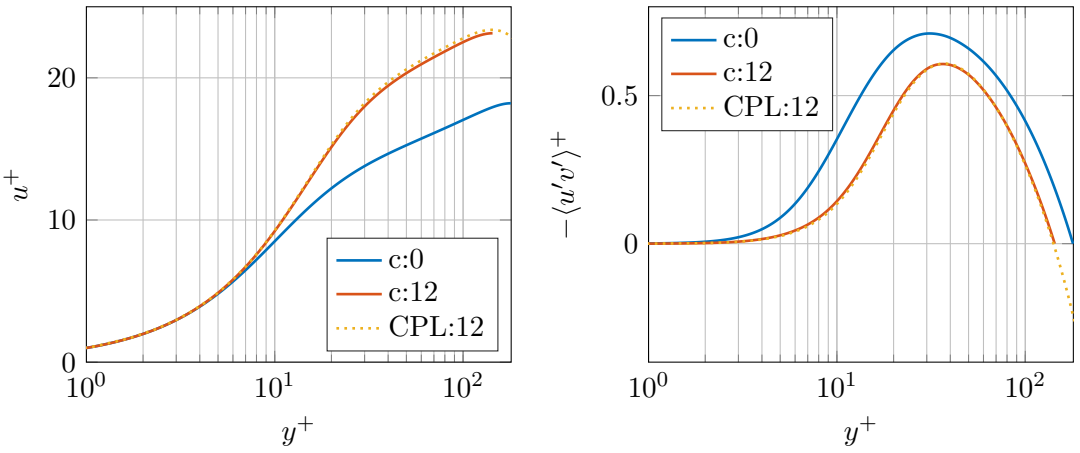

(a) (b)

Figure 5.3.: Mean streamwise velocity u^+ (a) and Reynolds stress $\langle u'v' \rangle / u_\tau^2$ (b) in the uncontrolled and controlled channel.

Moreover, the effects of the control technique are clearly visible. The streamwise velocity remains unchanged in the viscous sublayer $y^+ < 5$ and is elevated in the buffer layer $5 < y^+ < 30$ and the log-law region $y^+ > 30$. Note that the friction velocity of the controlled case was used for scaling of the controlled cases and the friction velocity of the uncontrolled cases was used for scaling of the uncontrolled case. As pointed out by Quadrio (2011) this is essential in order to be able to compare the controlled and uncontrolled flow. A similar behaviour for the controlled cases at $Re_\tau = 200$ was shown for instance by Baron and Quadrio (1995), Touber and Leschziner (2012) and by Ricco et al. (2012). The latter group applied a constant pressure gradient to drive the flow in order to avoid the problem of choosing the right scaling parameters.
The significant reduction of the Reynolds stress $\langle u'v' \rangle / u_\tau^2$ shown in 5.3 (b) was also presented by Touber and Leschziner (2012) for $Re_\tau = 500$.

The good agreement between the CPL and Nek5000 results is also shown in figure 5.4. The RMS values of the streamwise and wall-normal velocity fluctuations u^+_{rms}, v^+_{rms} are

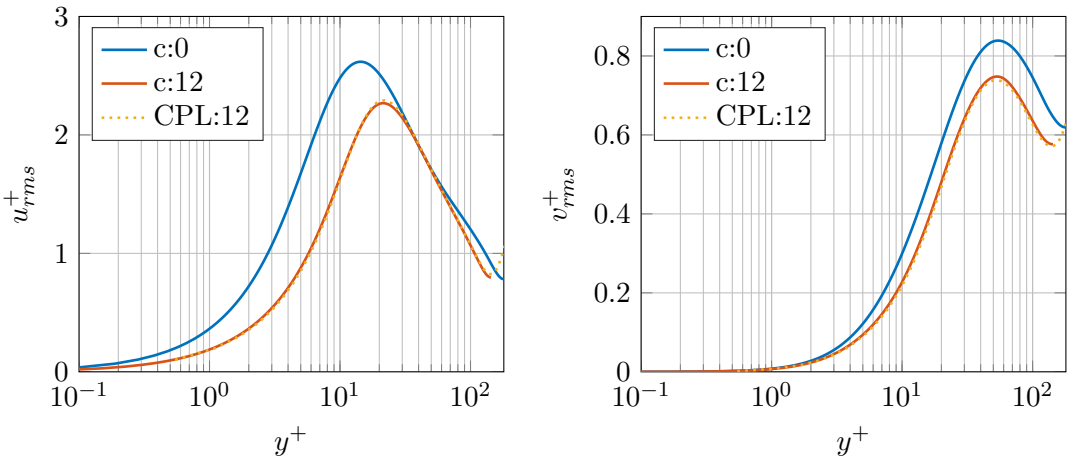

(a) (b)

Figure 5.4.: RMS of streamwise u^+_{rms} (a) and wall-normal v^+_{rms} (b) velocity fluctuations in the uncontrolled and controlled channel.

smaller than in the reference case. The peak of u^+_{rms} is slightly shifted away from the wall. These trends are also visible in Touber and Leschziner (2012) at $Re_\tau = 500$ and Ricco et al. (2012) at $Re_\tau = 200$.
Figure 5.5 shows the spanwise RMS velocity fluctuation. They are determined by the

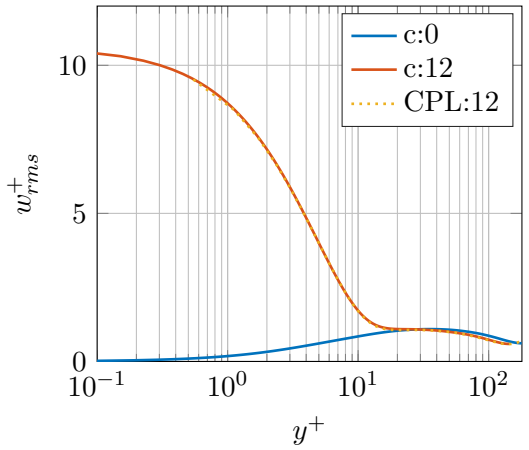

Figure 5.5.: RMS of spanwise velocity fluctuations w^+_{rms} in the uncontrolled and controlled channel.

amplitude of the wall velocity W_m in the region close to the wall. That is why the deviation of w^+_{rms} between the uncontrolled and controlled channel is very large up to approximately $y^+ = 10 - 20$. Touber and Leschziner (2012) and Ricco et al. (2012) apply a triple decomposition in order to filter the periodic component of the spanwise RMS velocity fluctuation out. Therefore, their results cannot be used for comparison but the agreement with the CPL results again is very good.
To sum up, the general agreement of every quantity which has been presented with data generated with a classical pseudo-spectral code (CPL) and data from the literature is good. Thus, the implementation is considered to be validated.

6. Results

In this chapter all major results of the turbulent duct cases are reported and discussed. The controlled cases are being compared to each other and to the uncontrolled case. A comparison to the channel flow is reported where appropriate.
The first section deals with results for the three mean velocities U, V, W the RMS values of their fluctuations u_{rms}, v_{rms}, w_{rms} and the Reynolds stresses $\langle u'v' \rangle$, $\langle u'w' \rangle$, $\langle v'w' \rangle$. Next, one of the objectives of this thesis, the effect of the applied flow control technique on secondary motions, is investigated. In the last section of this chapter the second objective of this thesis, the effect of the side walls on the performance of the flow control technique, is presented. Note that the non-dimensionalization was done with h and U_b as shown in section 2.3 and is used if nothing else is mentioned.

6.1. Mean statistics

First, 2D contour plots of the yz-plane and some selected wall-normal profile plots are presented. Due to symmetry reasons only one quarter of the duct flow is shown in each 2D contour plot. The first quarter on the upper right side shows the uncontrolled reference case denoted by d:0 where d abbreviates duct and 0 stands for the the uncontrolled case. The second quarter on the upper left side shows the first controlled duct case with an amplitude of wall velocity of $W_m^+ = 4.5$, denoted by d:4.5. The third quarter on the lower left side shows the second controlled duct case with an amplitude of wall velocity of $W_m^+ = 12$, denoted by d:12, and the last quarter on the lower right side shows the third controlled duct case with an amplitude of wall velocity of $W_m^+ = 4.5$ and only partially applied control to the horizontal walls, denoted by p:4.5. A more detailed description of all the investigated cases is given in chapter 4. The layout is depicted in figure 6.1.

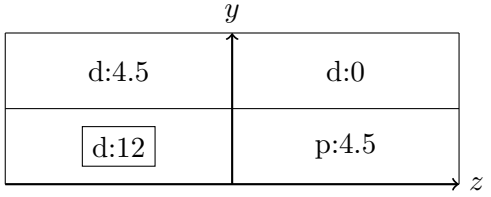

Figure 6.1.: Sketch of partitioning of 2D contour plots.

Note that appropriate symmetry conditions are used to compress and improve the information of the quarter on the lower left side only. Using the symmetries makes the results

more reliable. That major quarter on the lower left side is then expanded over the whole domain through mirroring at the symmetry axes. Thus, for some quantities their direction is not correct according to their quarter of the channel. For instance, the mean wall-normal velocity close to the side walls is negative in the upper part of the channel and positive in the lower part of the channel. The compressed and then expanded wall-normal velocity however is positive in all quarters because only the major quarter in lower left side is mirrored. Hence, one has to keep that in mind when interpreting the graphs. The advantage of this technique is that it facilitates the comparison between the different configurations because the same colour-map is used for all four cases. For clarity, every 2D contour plot is accompanied with a small sketch showing the major quarter in the lower left side and the sign of the other quarters, respectively.
In figure 6.2 the mean streamwise velocity U of the uncontrolled and the three controlled duct cases is presented. As expected, the velocity is zero at the walls and increases towards

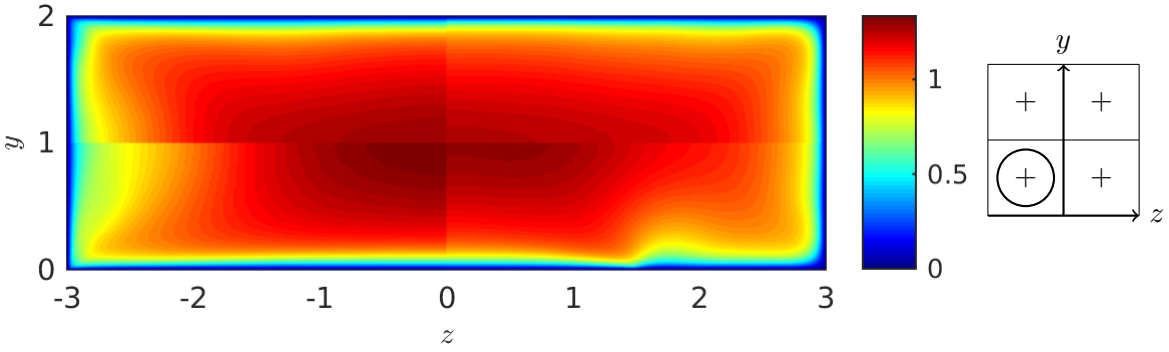

Figure 6.2.: Mean streamwise velocity of the four duct cases.

the centre. The difference between the uncontrolled flow and the first controlled case d:4.5 is very small. There is only a slight increase in the low-speed region at the side walls around $y \approx 1$. This low-speed region is further increased for the d:12 case which seems to be reasonable due to the wall movement being also increased (since this motion seems to produce this low-speed region). The results of the third controlled duct case p:4.5 in the lower right corner clearly show the end of the controlled region at $z = 1.5$. There is also a low-speed region around $1.5 < z < 2$ adjoining the end of the controlled region.
Moreover, a slightly different behaviour between the four cases can be seen at the corners. Whereas the uncontrolled duct case and the third one look very similar, the controlled duct cases d:4.5 and d:12 show a higher streamwise velocity close to the corners. For the third controlled duct case p:4.5 a region of higher velocity close to the walls can be found at $z \approx 1.5$.

To facilitate and complement comparison between the investigated cases, profile plots at two different spanwise positions were generated. In figure 6.3 profiles of the mean streamwise velocity at the centre of the channel / duct ($z = 0$) and at the region close to the wall ($z = -2.5$) are presented. The notation introduced in chapter 4 is used. Note that the scaling in viscous units is done by using the local friction velocity at the appropriate spanwise position. For the controlled cases the friction velocity of the actual case is used and not the uncontrolled friction velocity. The results for the uncontrolled and controlled channel case were already presented in chapter 5 but are kept in these plots for comparison.
Figure 6.3 (a) shows good agreement between the uncontrolled duct and channel case. Both curves coincide which means that the effect of the wall on the mean streamwise velocity at the centre is very little. Due to the applied control technique an upward shift of the profiles for the controlled cases starting from $y \approx 10$ is visible. The second controlled

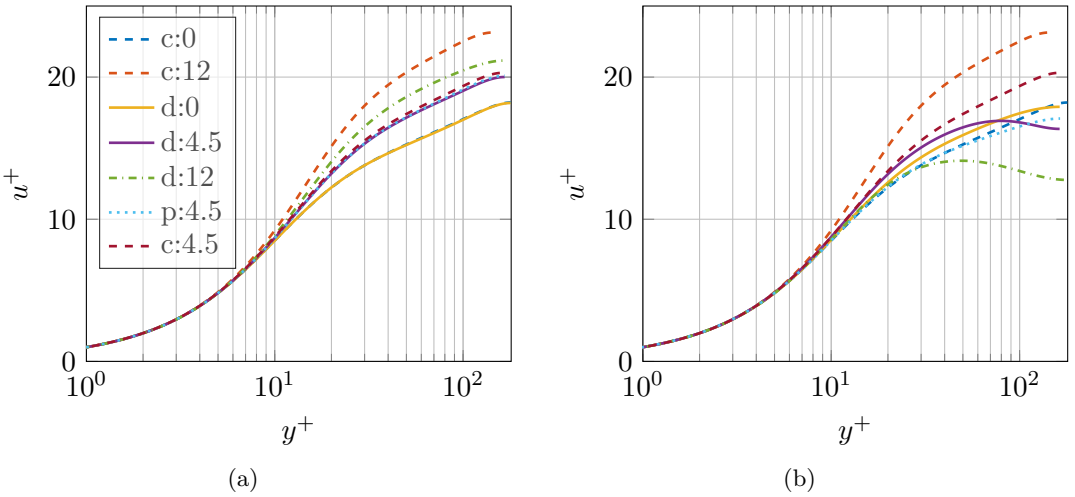

Figure 6.3.: Inner scaled mean streamwise velocity at $z = 0$ (a) and at $z = -2.5$ (b).

case d:12 is shifted further upwards than the first d:4.5 and third controlled case p:4.5 because of the higher wall amplitude velocity being used. The first, d:4.5, and third, p:4.5, controlled case almost coincide with the controlled channel case c:4.5.
The deviation between the controlled channel case c:12 and the second controlled duct case d:12 could originate from the influence of the side walls for the stronger amplitude of wall velocity of $W_m^+ = 12$. Both cases apply the same wall amplitude velocity. Hence, the same behaviour is expected in a region which is relatively far away from the wall. The small aspect ratio of 3 for the investigated duct cases seems to be too small to result in spanwise independence at the centre of the duct especially for the case d:12 with a high amplitude of wall velocity. All cases which apply $W_m^+ = 4.5$ show good agreement at the centre of the duct. Consequently, the influence of the side walls on the mean streamwise velocity appears to be small only for lower values of W_m^+.
The mean streamwise velocity profile close to the side walls at $z = -2.5$ is presented in figure 6.3 (b). Again, the uncontrolled duct case d:0 and the third controlled duct case p:4.5 are relatively similar. They mainly deviate from the reference channel case in a lower velocity at $y^+ \gtrsim 90$. As mentioned previously for the 2D streamwise velocity plot, the region of low-speed fluid close to the side walls can also be seen in that profile plot for the first, d:4.5, and second, d:12, controlled duct case.

The mean wall-normal velocity V is presented in figure 6.4. As mentioned in the beginning of this chapter the wall normal velocity in the upper half of the channel should be

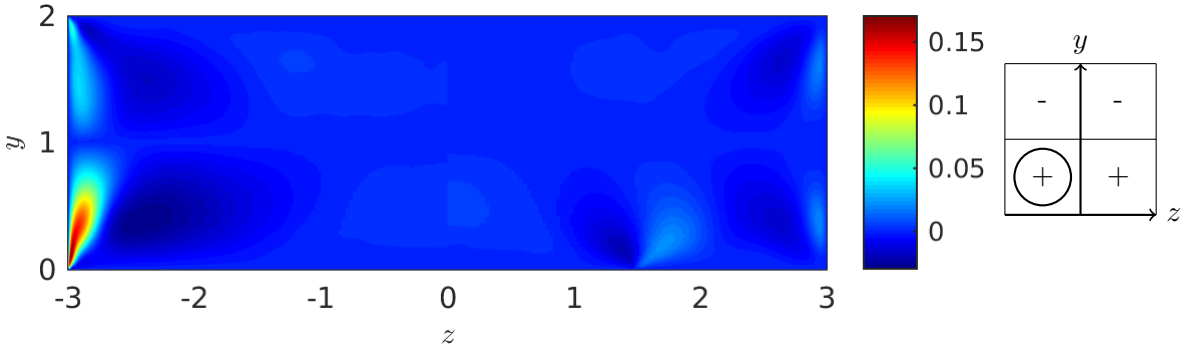

Figure 6.4.: Mean wall-normal velocity of the four duct cases.

multiplied by -1 to obtain the physical flow behaviour. For a better comparison of the magnitude this was not done but should be kept in mind when interpreting the results. Also, the signs are shown in the small sketch to the right of the 2D contour plot.
In the uncontrolled case the mean wall-normal velocity V appears to be very small everywhere except for a small region close to the side walls at $y \approx 1.5$. This increase of wall-normal velocity can be explained by the secondary flow induced by the side walls of the duct (Gessner and Jones, 1965). Next to the region of positive V close to the walls is a region of negative V closer to the centre of the channel. For the first, d:4.5, and especially the second controlled duct case, d:12, the wall-normal velocity is strongly increased at the side walls. The region of negative V intensifies and grows, too. Hence, the effect of the moving wall seems to strengthen the secondary flow. This will be further discussed in section 6.2. An explanation for the increased wall-normal velocity of the controlled cases d:4.5 and d:12 close to the side walls might be that fluid advected horizontally by the moving wall is being deflected vertically by the side wall. This event is much stronger than fluid being pulled down at the same phase of the oscillation at the other side wall. Therefore, on average V is increased close to the side walls.
The third controlled case again looks similar to the uncontrolled case at the area around the corner. Close to the end of the controlled area at $z = 1.5$ is a region of positive wall-normal velocity caused by the relatively abrupt end of the control area. This could explain the aforementioned low-speed region for the streamwise velocity at the same spanwise position because this positive wall-normal velocity convects low-speed streamwise fluid beneath it closer the core.

A comparison of the mean spanwise velocity W is given in figure 6.5. Again, a clue for the secondary flow of the uncontrolled case d:0 is visible. Fluid is being transported from the corner along the horizontal walls into the centre (red region in the upper right quarter). That red region is being pushed closer to the centre for the controlled duct cases d:4.5 and d:12. The region close to the corner for the controlled cases d:4.5 and d:12 shows fluid being transported to the corners along the horizontal wall due to the moving walls. Note that this is the opposite direction as for the uncontrolled flow. The dark blue and dark red regions in the lower left corner together with the information of the wall normal velocity in figure 6.4 indicate that a large clockwise rotating streamwise vortex is located at $z \approx -2.5$ and $y \approx 0.5$. This might explain the low-speed region of mean streamwise velocity mentioned earlier since this vortex pulls low-speed streamwise fluid from the side walls to the low-speed region.
The lower right quarter again shows similar behaviour as the uncontrolled case close to the corner. The change of sign of spanwise velocity at $z \approx 1.5$ in wall-normal direction could be caused by an anti-clockwise rotating streamwise vortex. Indications for such a vortex are also found in figure 6.4.

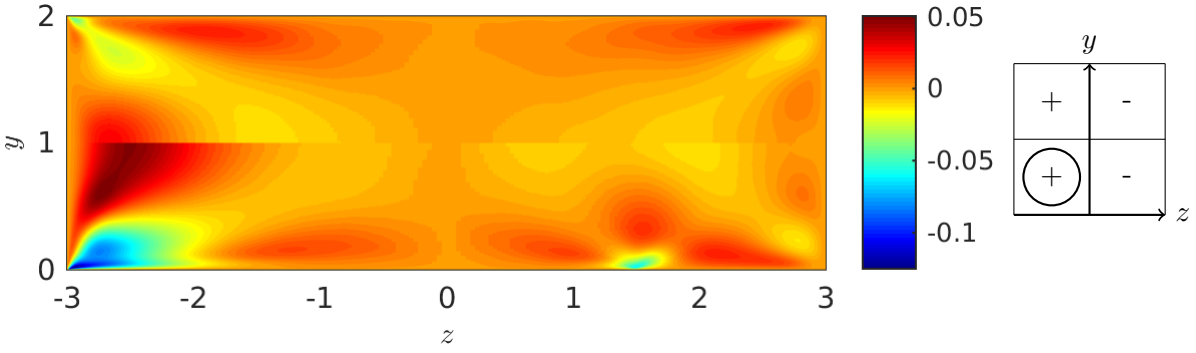

Figure 6.5.: Mean spanwise velocity of the four duct cases.

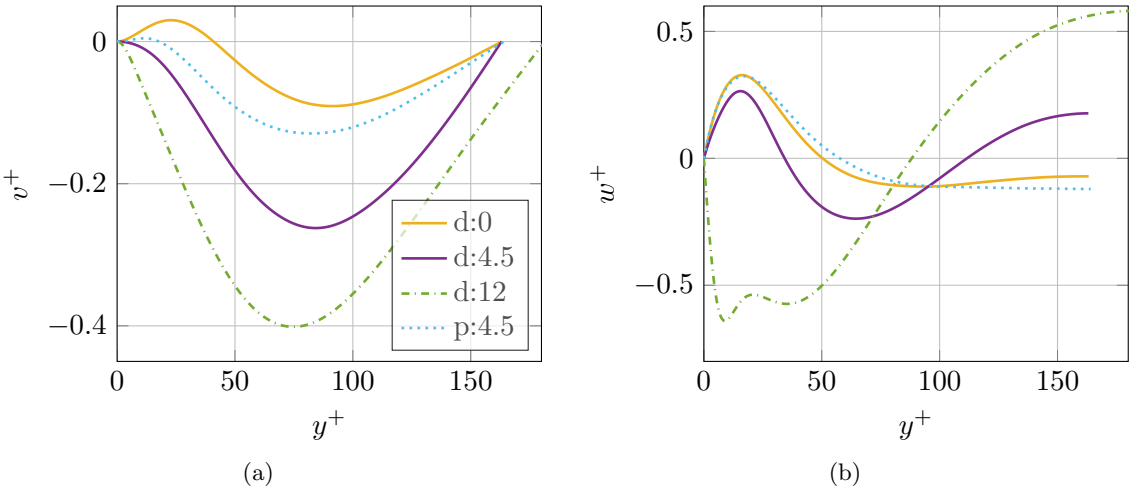

Figure 6.6.: Inner scaled mean wall-normal velocity (a) and mean spanwise velocity (b) at $z = -2.5$.

Figure 6.6 depicts the profiles of the mean wall-normal velocity v^+ (a) and spanwise velocity w^+ (b) at $z = -2.5$. At this specific spanwise location v^+ is mainly negative for all the duct cases. As shown in the 2D plot 6.4 fluid which is moved upwards close to the side walls is going down again at $z \approx -2.5$. In the uncontrolled duct case this motion is caused by the secondary flow. All duct cases tend to $v^+ = 0$ at the channel half height because the motions from the lower and the upper half of the channel cancel each other. Close to the side walls the third controlled duct case p:4.5 shows some deviations in v^+ to the uncontrolled duct case. The controlled cases d:4.5 and d:12 indicate a stronger downward motion at $z = -2.5$ which agrees with the increased upward motion even closer to the side walls. For the mean spanwise velocity at $z = -2.5$ shown in figure 6.6 (b) the uncontrolled duct case and the third controlled case p:4.5 show similar behaviour again. They have their peak value at $y^+ \approx 15$ before the direction changes at $y^+ \approx 40$ and then remains constant. The first controlled case d:4.5 shows a lower positive peak at $y^+ \approx 15$, a stronger negative peak at $y^+ \approx 60$ and a region of positive mean spanwise velocity again for $y^+ \gtrsim 110$. Moreover, the mean spanwise velocity is completely negative for the d:12 case in the first region $y^+ \lesssim 80$ lacking the first positive peak. The region of positive mean spanwise velocity starts already at $y^+ \approx 80$ for this case and the magnitude is higher than the d:4.5 case. This indicates that there is a strong vortex at this position as already mentioned for the 2D plot.

The next investigated quantity is the RMS of the streamwise velocity fluctuation u' displayed in figure 6.7. The uncontrolled case d:0 shows areas along the horizontal and side wall of high u_{rms}. The controlled cases d:4.5 and d:12 reduce the RMS of fluctuating streamwise velocity along the moving horizontal wall but along the side walls it is increased. For the second controlled duct case d:12 in the lower left corner this area of strongly increased u_{rms} at the side wall appears to influence the whole quarter even up to the core region. The blue region of small u_{rms} which is very much alike for controlled case d:4.5 and the uncontrolled case d:0 is much reduced in the second control case d:12. Therefore, for the case of high amplitude of wall velocity $W_m^+ = 12$ the side walls seem to affect the flow even in the core region. The third controlled duct case clearly shows the sudden stop of the controlled area by the region of increased streamwise velocity fluctuations next to $z = 1.5$. Along the controlled area however the expected decrease due to the applied control technique (Touber and Leschziner, 2012) is found.
A closer look at the RMS value of the streamwise fluctuating velocity at spanwise position

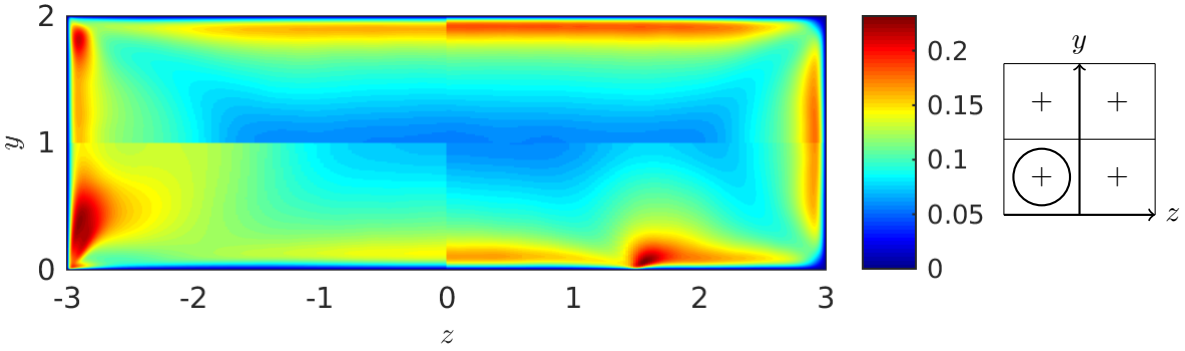

Figure 6.7.: RMS of streamwise velocity fluctuations of the four duct cases.

$z = 0$ (a) and $z = -2.5$ (b) is presented by profile plots in figure 6.8. At $z = 0$ the uncontrolled duct case d:0 and the uncontrolled channel flow c:0 are very similar. The

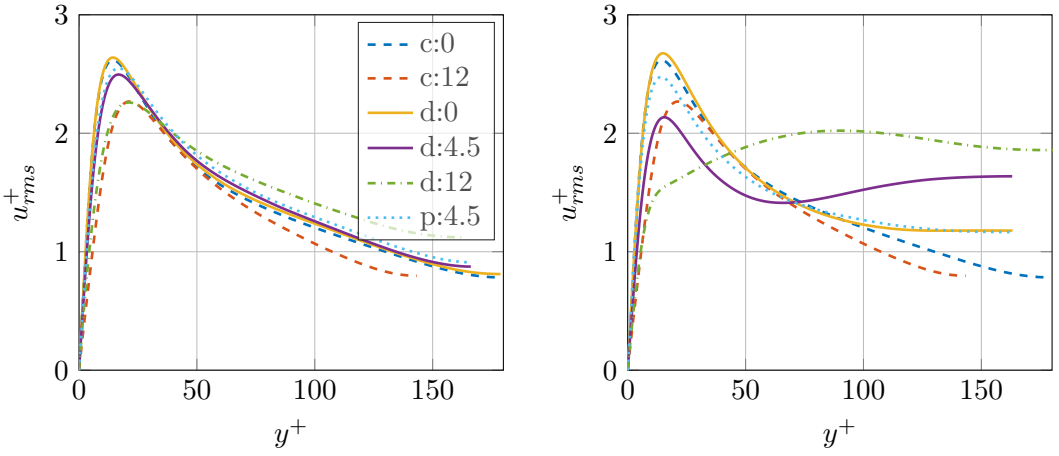

Figure 6.8.: Inner scaled RMS of fluctuating streamwise velocity at $z = 0$ (a) and at $z = -2.5$ (b).

controlled channel case c:12 and the second controlled duct flow d:12, which share the same amplitude of wall velocity, show a reduction and a slight shift of their peak value to higher y^+. However, after this reduced peak the RMS value for the second controlled duct case d:12 is larger than for the controlled channel case c:12 and even larger than for the uncontrolled reference case d:0. Controlled cases d:4.5 and p:4.5 show a slight reduction of the peak value but apart from that almost coincide for higher y^+ with the uncontrolled case d:0. Hence, u^+_{rms} in the core region is mostly unaffected by the applied control technique for low W^+_m as already pointed out for the 2D contour plot 6.7.
Closer to the side walls at $z = -2.5$ the profile of the uncontrolled duct case d:0 is similar to the uncontrolled channel case c:0 except for $y^+ \gtrsim 100$ where u^+_{rms} is higher for the duct case. The controlled case d:4.5 shows a strong reduction of the peak value but also a region of increased u^+_{rms} for $y^+ \gtrsim 70$ compared to the uncontrolled case d:0. A further increased value of u^+_{rms} for higher y^+ can be seen for the controlled duct case d:12 which does not resemble the behaviour of the corresponding channel case c:12 anymore. There is only a slight reduction between $0 \lesssim y^+ \lesssim 70$ for p:4.5 compared to the reference case d:0.

In figure 6.9 the RMS value of the wall-normal velocity fluctuation is displayed. The region at the side walls for the controlled cases d:4.5 and d:12 is increased compared to the

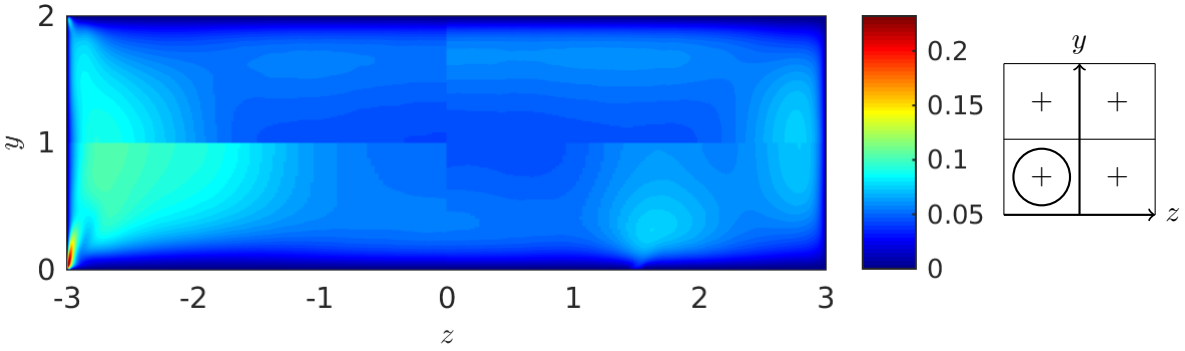

Figure 6.9.: RMS of wall-normal velocity fluctuations of the four duct cases.

uncontrolled case. Furthermore, there is a very strong region located at the corner of the second control case d:12. The third controlled case p:4.5 shows the a region of increased v_{rms} next to the controlled area.
That behaviour of u_{rms} and v_{rms} indicates already that the side walls can have a strong effect on the overall efficiency of the applied control technique. The regions of increased velocity fluctuations at the side-walls do not exist in the channel flow.

Figure 6.10 presents the profile plots of the RMS of the wall-normal velocity fluctuation again at two different spanwise locations $z = 0$ (a) and $z = -2.5$ (b) compared to the channel cases. The profiles at the centre of the duct in figure 6.10 (a) show that un-

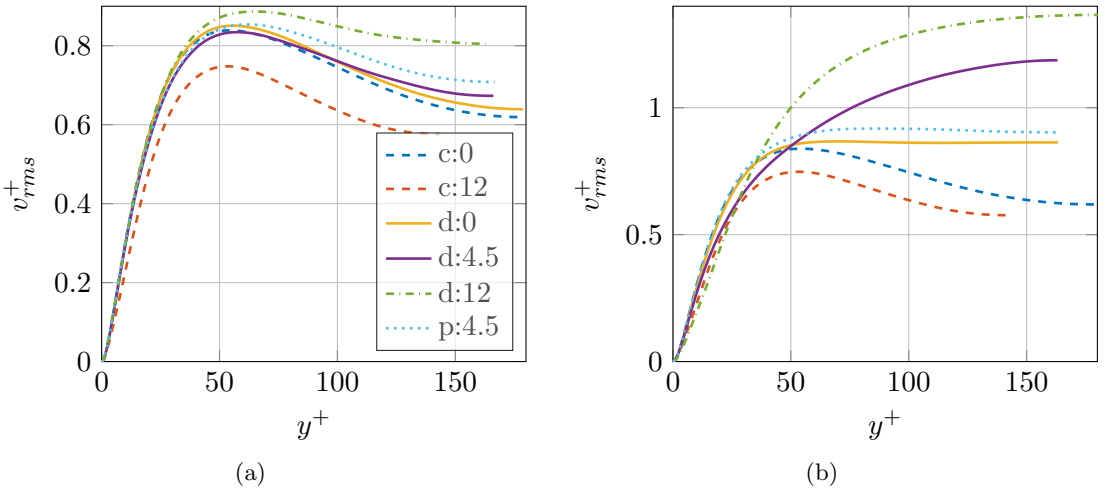

Figure 6.10.: Inner scaled RMS of fluctuating wall-normal velocity at $z = 0$ (a) and at $z = -2.5$ (b).

controlled channel c:0 and duct case d:0 bear close resemblance. However, the controlled duct cases do not show a reduction of v^+_{rms} as can be seen for the channel flow c:12. On the contrary, the controlled duct cases d:12 and p:4.5 show an increase in v^+_{rms} and case d:4.5 only changes slightly compared to the uncontrolled case.
For the spanwise location closer to the side-wall at $z = -2.5$ this trend becomes even stronger. First, the influence of the side wall raises v^+_{rms} in the uncontrolled duct case d:0 at $y^+ \gtrsim 55$ over the level of the uncontrolled channel case c:0. The applied control technique seems to amplify v^+_{rms} close to the side wall as already shown in 6.9.

Since the fluctuating part of the velocity is computed by the Reynolds decomposition stated in equation 2.8 the periodic part of the wall movement is still part of the fluctuat-

ing value. Thus, the oscillation of the wall dominates the spanwise velocity fluctuations as can be seen in figure 6.11. Even though only the high value at the horizontal walls can be

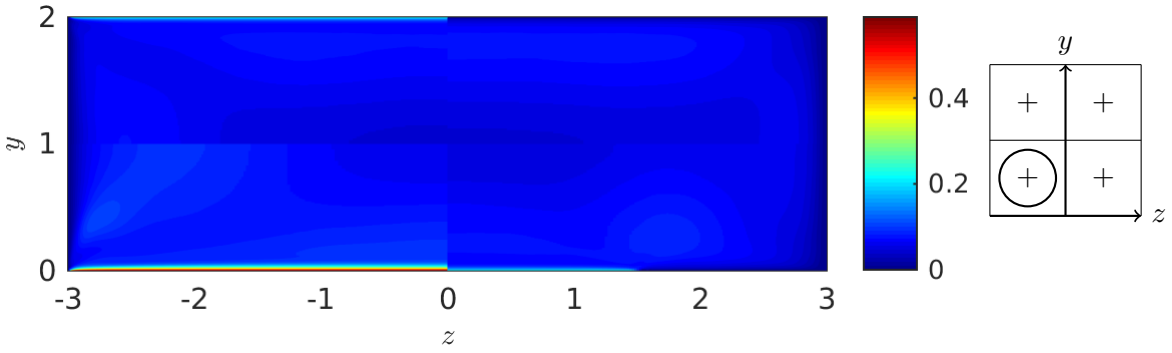

Figure 6.11.: RMS of spanwise velocity fluctuations of the four duct cases.

seen this 2D plot is kept for completeness. The profile plots in figure 6.12 show that peak at the horizontal walls too but facilitate the comparison of different cases with each other. Note that even though the same wall amplitude velocity is used for the controlled channel

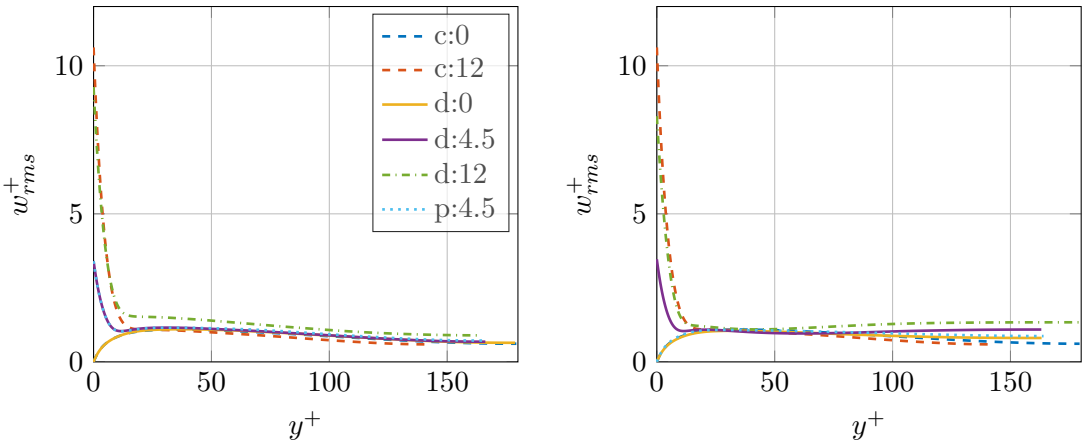

Figure 6.12.: Inner scaled RMS of fluctuating spanwise velocity at $z = 0$ (a) and at $z = -2.5$ (b).

case c:12 and the second controlled duct case d:12 the RMS of the spanwise fluctuating velocity does not necessarily have to be the same at the wall. That is because for these plots the scaling with the local friction velocity of the actual case is used whereas the wall amplitude velocity is scaled with the averaged friction velocity of the uncontrolled cases respectively.
The periodic part induced by the control technique dominates the w^+_{rms} behaviour close to the horizontal wall at $y^+ \lesssim 20$. At $z = 0$ the uncontrolled channel c:0 and duct cases d:0 coincide as well as the controlled duct cases d:4.5 and p:4.5 which share the same amplitude of wall velocity. The reduction in w^+_{rms} in the region not dominated by the wall oscillation $y^+ \gtrsim 20$ for the controlled channel flow c:12 cannot be found for the controlled duct cases. Interestingly, the second controlled duct case d:12 does not fall back to the level of the uncontrolled duct case d:0 and remains larger even for the region of $y^+ \gtrsim 20$. Closer to the side wall at $z = -2.5$ the uncontrolled d:0 and the third controlled duct case p:4.5 almost coincide again and only differ from the uncontrolled channel case c:0 at $y^+ \gtrsim 100$ with larger values. The controlled cases d:4.5 and d:12 are even more increased.

As discussed in section 2.5 the turbulent contribution to the skin-friction coefficient in a fully-developed turbulent channel solely depends on the Reynolds stress $\langle u'v' \rangle$ and its distribution in wall normal direction. Even though the different contributions to the skin-friction coefficient are not as easily identified in the fully developed turbulent duct flow a similar behaviour is expected at the centre plane, at least for wide enough ducts.
A slight reduction of the magnitude of the Reynolds stress $\langle u'v' \rangle$ between the uncontrolled case d:0 and the first controlled case d:4.5 can be seen along the horizontal wall in figure 6.13. The second controlled duct case d:12 also shows a reduction in magnitude in the

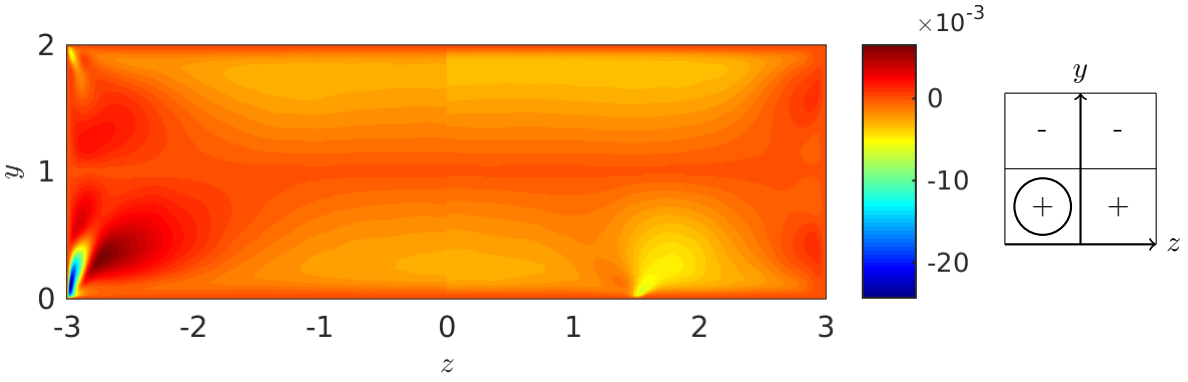

Figure 6.13.: Reynolds stress $\langle u'v' \rangle$ of the four duct cases.

core region. Interestingly, there is a region of positive $\langle u'v' \rangle$ adjoining the negative core region for the d:12 case. This would result in a skin-friction coefficient C_f even smaller than the laminar one according to equation 2.43 as the second term in this equation will be negative. However, the simple decomposition of the skin-friction coefficient in equation 2.43 is not valid for the duct anymore, particularly not close to the side walls.
At the corner a strongly negative region is found again indicating that wall shear stress might be much increased at this location. The third control case p:4.5 also shows a reduction of $\langle u'v' \rangle$ compared to the uncontrolled case d:0 up until the end of the control area at $z = 1.5$. Adjacent to the controlled area there is a region of increased magnitude of $\langle u'v' \rangle$.
Investigating the profiles at $z = 0$ in figure 6.14 (a) yields a slightly increased $\langle u'v' \rangle^+$ of the

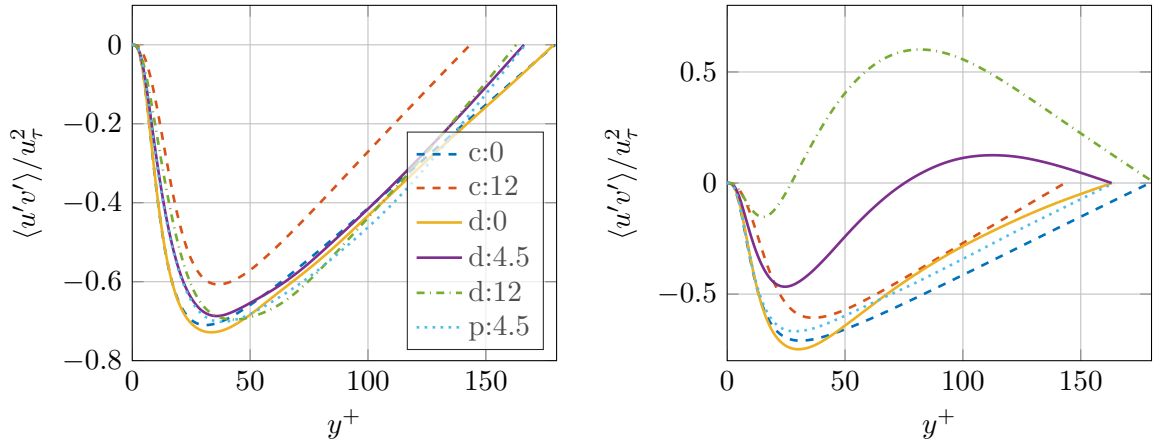

Figure 6.14.: Reynolds stress $\langle u'v' \rangle / u_\tau^2$ at $z = 0$ (a) and at $z = -2.5$ (b).

uncontrolled duct case d:0 compared to the uncontrolled channel case c:0. The reduction for the first controlled duct case d:4.5 is visible but much smaller than for the controlled channel case. The second, d:12, and third, p:4.5, controlled duct case are even increased

in the region of $50 < y^+ < 110$ and $50 < y^+ < 130$ respectively.
As already visible in the 2D plot a large region of positive $\langle u'v' \rangle^+$ is found for the first, d:4.5, and especially the second, d:12, controlled duct case at $z = -2.5$ in figure 6.14 (b).

The next statistical quantity presented is the Reynolds stress $\langle u'w' \rangle$. Figure 6.15 shows that the magnitude of this quantity is increased by the applied control technique. Very

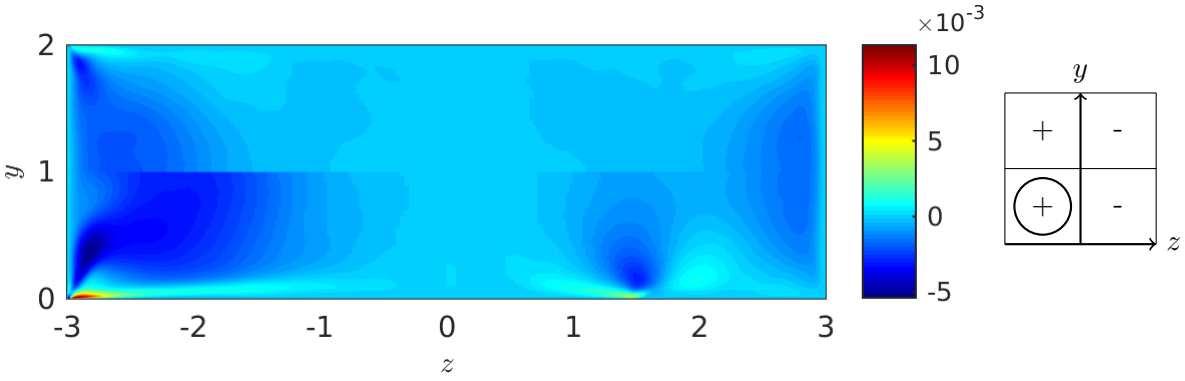

Figure 6.15.: Reynolds stress $\langle u'w' \rangle$ of the four duct cases.

strong effects are found again at the corners for controlled cases d:4.5 and d:12 and at the end of the controlled area for the case p:4.5. At least for a duct with very large height one would expect that at its half height this could be treated as a channel again and that $\langle u'w' \rangle$ and its distribution in spanwise direction solely determine the turbulent contribution to the skin-friction drag as discussed in section 2.5. Then, a reduction of $-\langle u'w' \rangle$ would be desired in order to reduce drag. Even though this is clearly not the case for the investigated geometry the increase in magnitude of $\langle u'w' \rangle$ might be disadvantageous considering overall drag reduction. Furthermore, a comparably very strong and small positive region close to the corner of d:12 can be found which is probably caused by the relatively abrupt stop of the moving wall region. Such a region of positive $\langle u'w' \rangle$ is also found for d:4.5 and a negative region for p:4.5. Interestingly, the magnitude for p:4.5 in this region is higher even though the same amplitude of wall velocity is used in both cases.

A profile plot of the Reynolds stress $\langle u'w' \rangle^+$ at $z = -2.5$ is displayed in figure 6.16. The uncontrolled case d:0 and the third controlled case p:4.5 are relatively similar again.

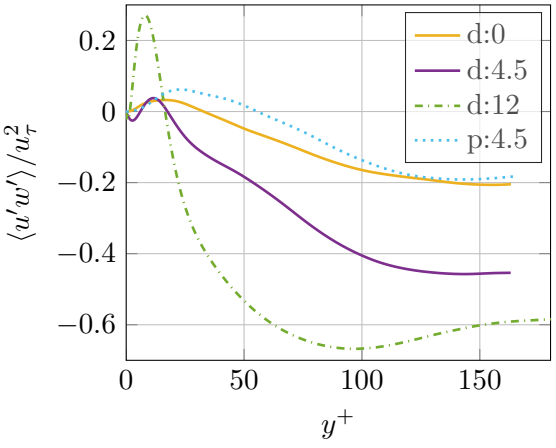

Figure 6.16.: Reynolds stress $\langle u'w' \rangle / u_\tau^2$ at $z = -2.5$.

The controlled duct cases d:4.5 and d:12 show intensified regions of $\langle u'w' \rangle^+$ and a positive peak which seems to increase with the applied wall amplitude velocity.

For completeness, the 2D contour plot of the Reynolds stress $\langle v'w' \rangle$ is also presented in figure 6.17. The dominating region is again the corner of the second controlled case d:12

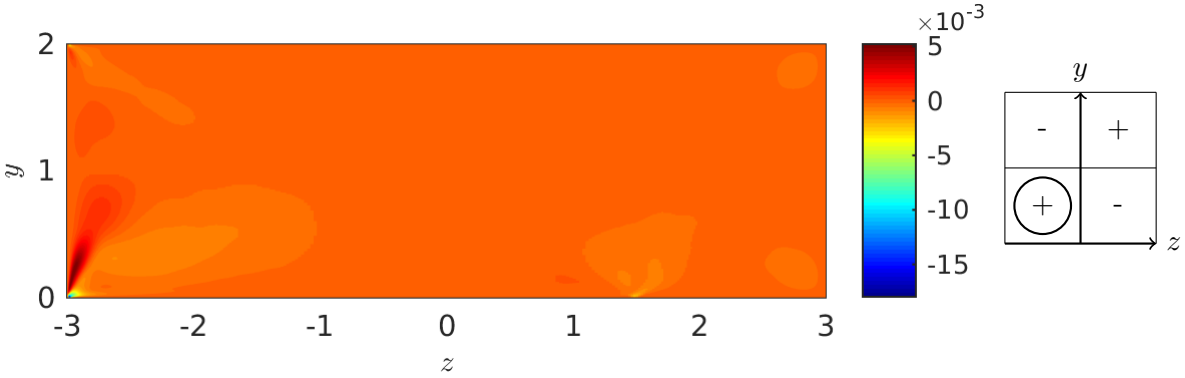

Figure 6.17.: Reynolds stress $\langle v'w' \rangle$ of the four duct cases.

with the maximum value located close to the side wall and the minimum located close to the corner along the horizontal wall. Similar but weaker features are found for the first controlled case d:4.5 and a region of positive $\langle v'w' \rangle$ at the end of the controlled section in case p:4.5.

6.2. Secondary flow

One remarkable feature of the turbulent flow in a rectangular duct is the presence of the secondary flow field. As explained in section 2.4 this is a flow normal to the streamwise direction. The secondary flow is visualized by use of the kinetic energy of the secondary flow given in equation 2.42 determining the colour of 2D contour plots. Note that the non-dimensionalized wall-normal and spanwise velocities were used to compare the kinetic energy. Additionally, in-plane streamlines and in-plane velocity vectors are presented to show the shape and direction of the generated vortices.
As in the previous chapter, appropriate symmetry conditions are used to improve the statistics and a compact visualization of all four duct cases is shown in figure 6.18. The

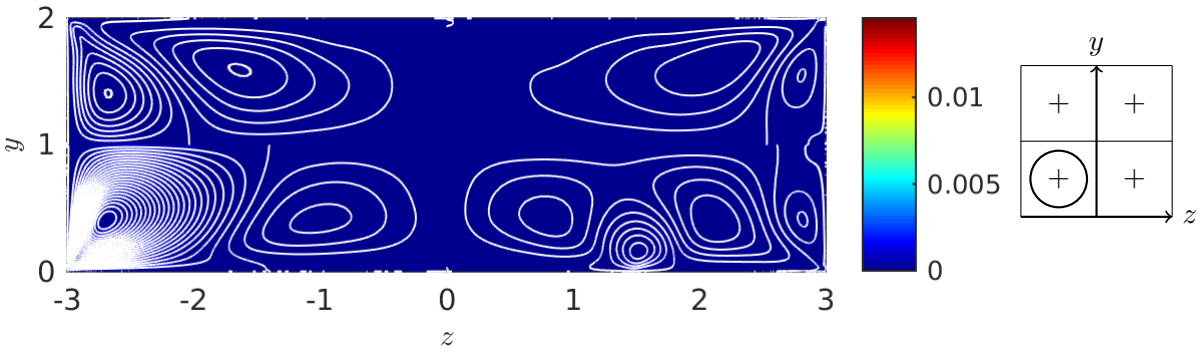

Figure 6.18.: Secondary flow field of all four duct cases using the same scaling for streamlines and contour plot.

partitioning is kept the same as in the previous section and shown in figure 6.1 with the uncontrolled duct case d:0 in the upper right corner, d:4.5, d:12 and p:4.5 following in anti-clockwise direction. In order to be able to compare the four cases to each other the colour-map indicating the magnitude of the kinetic energy of the secondary flow as well as the spacing of the streamlines shown in white are kept constant over all four cases.
It is evident from the in-plane streamlines that the second controlled duct case d:12 in the lower left corner features a very strong vortex at the corner. The maximum of the kinetic energy of the secondary flow is covered by the tightly distributed streamlines. The kinetic energy of the secondary flow in that case is much larger than in the other cases and consequently outshines them.
Moreover, the secondary flow in d:12 is peculiar because this very strong vortex at the corner seems to push its counter rotating vortex partner further into the core region of the duct. A similar but weaker behaviour can also be found for d:4.5 where the vortex at the side wall is intensified too and the centre of its counter rotating vortex partner is also pushed closer to the core region than in the uncontrolled case.
The third controlled case p:4.5 features an additional vortex pair: one at the end of the controlled region and its partner next to it closer to the centre of the duct.

Figure 6.18 clearly shows the different magnitudes of the secondary flow by the in-plane streamlines with the same spacing applied. However, the specific details of each case are obscured by this same scaling. Therefore, each of the four duct cases is explained separately, starting with the uncontrolled duct case d:0 displayed in figure 6.19. Due to symmetry reasons only the lower left corner is shown. The in-plane streamlines clearly show the typical pair of counter rotating vortices for the uncontrolled duct case. The vortex located at the side wall is smaller because the other one can spread in spanwise direction. The direction of the vortices is indicated by the arrows. As described in section 2.4 the secondary motions transport momentum from the core region to the corner bisectors.

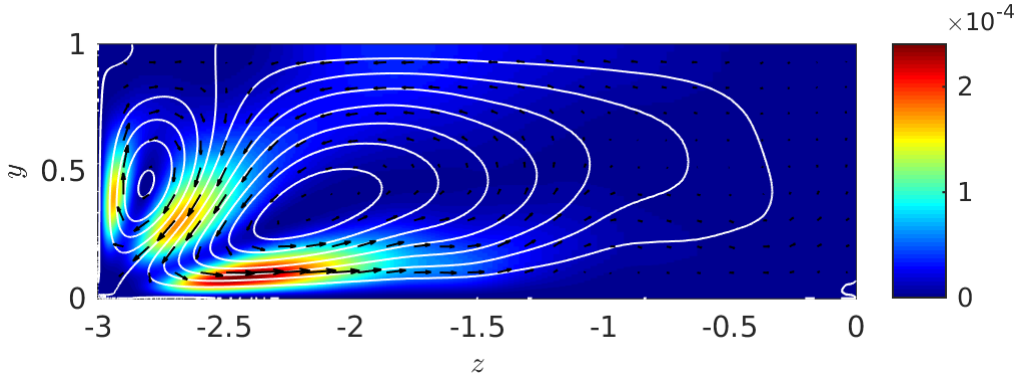

Figure 6.19.: Kinetic energy of the secondary flow K of the uncontrolled duct case d:0.

Close inspection of the 2D contour plot of the mean streamwise velocity in figure 6.2 also shows this transport of high streamwise velocity towards the corner caused by the secondary motions. Effects of this pair of vortices can also explain regions of intensified mean wall-normal and mean spanwise velocity in the 2D plots in figures 6.4 and 6.5.
The kinetic energy of the secondary flow displays three regions of high K with the maximum of $K_{max} = 2.4 \cdot 10^{-4}$ on the horizontal wall at $z \approx -2.4$. Following the approach by Vinuesa et al. (2015) the average kinetic energy of the secondary flow is calculated for the window at $0 < y < 2$ and $-3 < z < -2$ and denoted by $\langle K_{yz1} \rangle$. Its value is $\langle K_{yz1} \rangle = 4.7 \cdot 10^{-5}$. This agrees well with their given data and indicates that the averaging time was long enough. The average value over the whole cross section is given by $\langle K_{yz} \rangle = 2.4 \cdot 10^{-5}$. A comparison shows that approximately 65% of the kinetic energy of the secondary flow is contained within this first window. Those scalar values are summarized for all the different cases in table 6.1.

Table 6.1.: Comparison of scalar values of the kinetic energy of the secondary flow field.

	d:0	d:4.5	d:12	p:4.5
K_{max}	$2.404 \cdot 10^{-5}$	$1.384 \cdot 10^{-3}$	$1.457 \cdot 10^{-2}$	$1.814 \cdot 10^{-3}$
$\langle K_{yz} \rangle$	$2.377 \cdot 10^{-5}$	$7.772 \cdot 10^{-5}$	$5.239 \cdot 10^{-4}$	$5.493 \cdot 10^{-5}$
$\langle K_{yz1} \rangle$	$4.698 \cdot 10^{-5}$	$1.690 \cdot 10^{-4}$	$1.384 \cdot 10^{-3}$	$5.264 \cdot 10^{-5}$

The kinetic energy of the secondary flow for the first controlled duct case d:4.5 is displayed in figure 6.20. Note that the spacing of the in-plane streamlines and the colour-map are

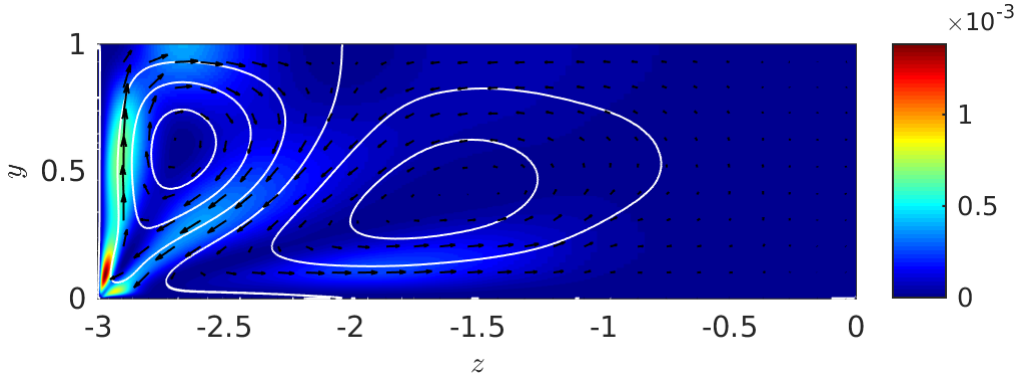

Figure 6.20.: Secondary flow field of the controlled duct case d:4.5.

different compared to the previous plot. The characteristic pair of counter rotating vortices is still present. However, the one at the side wall is intensified by the applied control technique. This can also be seen directly at the 2D contour plots of the mean wall-normal

velocity and spanwise velocity in figures 6.4 and 6.5 already. The intensified region of mean wall-normal velocity in the vicinity of the side wall results in an amplification of the strength of the associated vortex.
The other vortex appears to be amplified and increased in size too even though the adjusted scaling seems to indicate the opposite. In order to compare the in-plane streamlines of this controlled case with the uncontrolled case figure 6.18 must be employed.
The location of the maximum changes from the horizontal wall to the side wall, closer to the corner and increases to $K_{max} = 1.384 \cdot 10^{-3}$. This maximum is caused by the deflection of the fluid being advected towards the side wall. Hence, the mechanism leading to the formation of this vortex is different compared to the secondary flow of the uncontrolled duct case which is induced by the Reynolds stresses $\langle v'^2 \rangle$, $\langle w'^2 \rangle$, $\langle v'w' \rangle$ as described in section 2.4. Consequently, this secondary flow is not necessarily exclusively present in turbulent flows even though high values of the according Reynolds stresses can be found at the corner. It would be interesting to test whether those vortices induced by the control technique are present in a laminar case as well.
The averaged kinetic energy of the secondary flow in the whole cross section and in the first window also increase to $\langle K_{yz} \rangle = 7.8 \cdot 10^{-3}$ and $\langle K_{yz1} \rangle = 1.7 \cdot 10^{-4}$. This leads to the conclusion that approximately 74% of the kinetic energy of the secondary flow is contained in the first window.

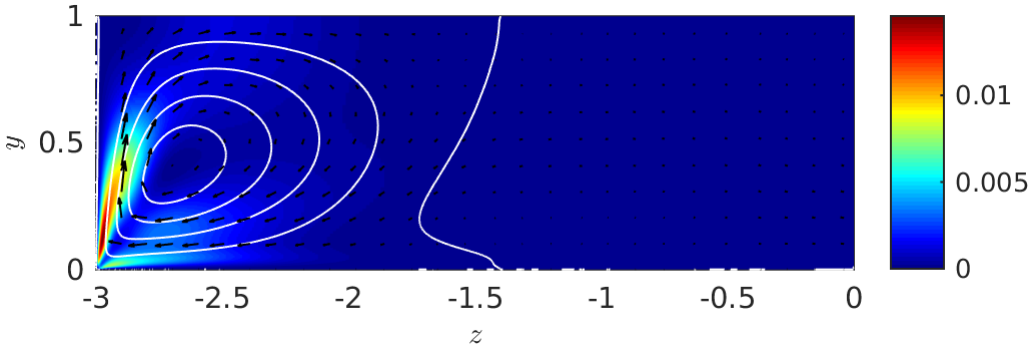

Figure 6.21.: Secondary flow field of the controlled duct case d:12.

Figure 6.21 presents the secondary flow field of the controlled duct case d:12. The vortex at the side wall increased in size compared to the case with lower wall velocity d:4.5. Its counter rotating vortex partner is much weaker and consequently not displayed by the streamlines anymore. It still exists though as can be seen in figure 6.18. Interestingly, the maximum value of the kinetic energy of the secondary flow $K_{max} = 1.5 \cdot 10^{-2}$ is about one order of magnitude larger than for the d:4.5 case. The same can be found for the overall average $\langle K_{yz} \rangle = 5.2 \cdot 10^{-4}$ and $\langle K_{yz1} \rangle = 1.4 \cdot 10^{-3}$. In this case approximately 90% of the kinetic energy of the secondary flow is contained within the first window.
As before, indications for this strong vortex can also be found in the 2D contour plots 6.4 and 6.5. This vortex structure also explains the low-speed region identified in figure 6.2 since low-speed fluid is convected from the wall into this region by the vortex. Moreover, regions of high Reynolds stresses $\langle v'^2 \rangle$, $\langle w'^2 \rangle$ and $\langle v'w' \rangle$ are also found at the corners.

The kinetic energy of the secondary flow of the last controlled duct case p:4.5 is shown in figure 6.22. Due to the fact that the control area does not end in the corner, the two vortex formation mechanisms are decoupled. At the corner a similar structure of a pair of vortices convecting momentum towards the bisector as for the uncontrolled case is found. The second vortex of this pair, which is closer to the core region, is squeezed in spanwise direction by the other pair of vortices. Interestingly, the maximum value of the secondary

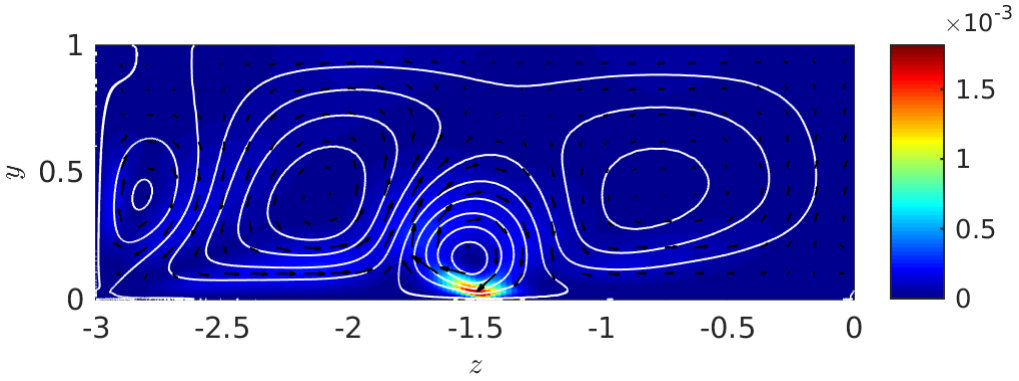

Figure 6.22.: Secondary flow field of the controlled duct case p:4.5.

flow for this case $K_{max} = 1.8 \cdot 10^{-3}$ and the overall average $\langle K_{yz} \rangle = 5.5 \cdot 10^{-5}$ are approximately the same order as for the d:4.5 case (see table 6.1). The maximum is approximately 29% larger and the overage over the whole cross section is 29% smaller than the respective ones for the d:4.5 case.
The kinetic energy of the secondary flow in the first window $\langle K_{yz1} \rangle = 5.3 \cdot 10^{-5}$ is smaller than for the d:4.5 case because only the pair of vortices at the corner is captured in the first window. The other pair of vortices induced by the oscillation of the wall might strengthen the corner vortices by driving the adjoining one. This leads to the slightly increased $\langle K_{yz1} \rangle$ compared to the uncontrolled duct case (see table 6.1).

6.3. Wall shear stress and drag reduction

The second objective of this thesis is to investigate the effect of the applied control technique on drag reduction. The effect of the control on the wall shear stress is directly related to drag reduction by equation 2.44. Therefore, the global effects of the investigated control technique are presented. Additionally, the behaviour of the wall shear stress along the walls will be discussed to better understand the different contributions to the global effect. First, the global drag reduction achieved by applying the control technique for the controlled channel and duct cases is shown in figure 6.23. Here, the global drag reduction

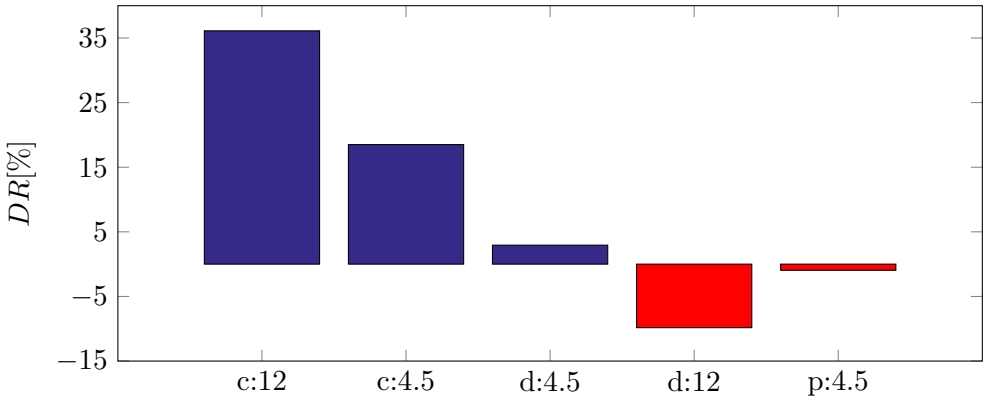

Figure 6.23.: Global drag reduction for each controlled case.

for the duct cases is calculated by using global friction coefficients which are a weighted average of the friction coefficient on the vertical and horizontal walls of the duct.
The total drag reduction for the controlled channel cases c:12 and c:4.5 are $DR = 36.1\%$ and $DR = 18.5\%$, respectively. Compared to the relatively high drag reduction levels of the channel cases the results in the duct cases are poor. The only controlled duct case which yields positive drag reduction is d:4.5 with $DR = 2.94\%$. The oscillation of the walls for the other two controlled duct cases d:12 and p:4.5 results in a negative drag reduction of $DR = -9.83\%$ and $DR = -0.95\%$. A comparison of those scalar values related to drag reduction for all the investigated cases is given in table 6.2.

Table 6.2.: Comparison of wall shear stress related scalars between all investigated cases.

		c:0	c:12	c:4.5	d:0	d:4.5	d:12	p:4.5
Re_b		2800	2800	2800	2581	2581	2581	2581
$Re_b(z=0)$		2800	2800	2800	2786	2843	2973	2863
Re_τ		179.3	143.3	161.9	165.8	163.3	173.7	166.6
$Re_\tau(z=0)$		179.3	143.3	161.9	178.8	166.2	162.8	166.7
τ_w	$[\cdot 10^{-3}]$	4.102	2.621	3.343	4.125	4.004	4.531	4.164
$\tau_w(z=0)$	$[\cdot 10^{-3}]$	4.102	2.621	3.343	4.799	4.145	3.980	4.173
$\tau_{w,hor}$	$[\cdot 10^{-3}]$	4.102	2.621	3.343	4.310	4.010	4.697	4.412
$\tau_{w,ver}$	$[\cdot 10^{-3}]$	0	0	0	3.571	3.726	4.032	3.420
DR	[%]	0	36.1	18.5	0	2.94	−9.83	−0.95
DR_{hor}	[%]	0	36.1	18.5	0	4.95	−8.99	−2.38
DR_{ver}	[%]	0	0	0	0	−4.34	−12.9	4.24

Unlike in the channel cases, the side walls also contribute to the global friction coefficient in the duct cases. Figure 6.24 displays the drag reduction levels on the horizontal walls (a) and the drag reduction levels of the duct cases on the side walls (b). Additionally, p:4.5in displays the drag reduction of controlled case p:4.5 evaluated only at the inner

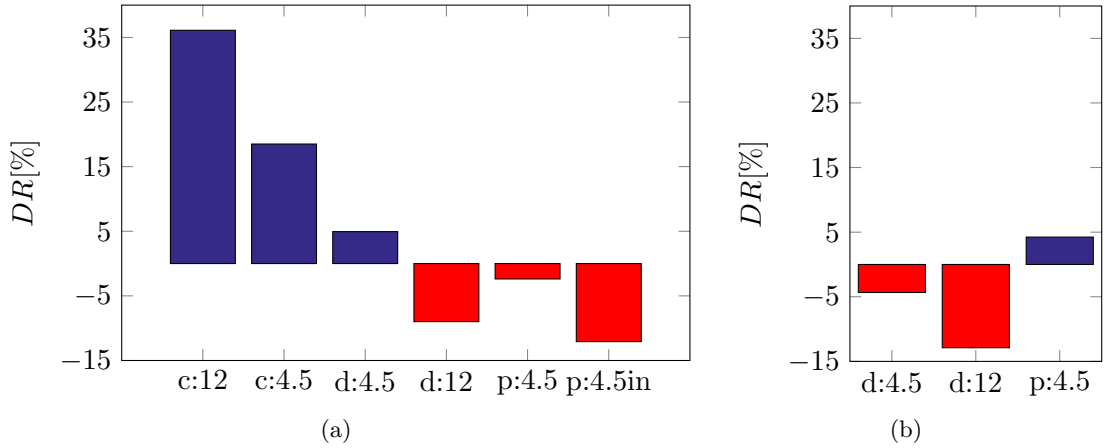

Figure 6.24.: Drag reduction at the horizontal walls (a) and the vertical walls (b).

region $-1.5 < z < 1.5$, where the control technique is actually applied.
The drag reduction level for the controlled duct case d:4.5 along the horizontal walls is $DR_{hor} = 4.95\%$ but at the vertical walls there is a drag increase compared to the uncontrolled case of $DR_{ver} = -4.34\%$. Hence, the small improvement at the horizontal walls is damped by the increased friction at the side walls. The second controlled duct case d:12 already shows a negative drag reduction level at the horizontal walls of $DR_{hor} = -8.99\%$. Additionally, increased friction at the side walls results in a strong drag increase of $DR_{ver} = -12.9\%$. The third controlled duct case p:4.5, which only applies the control technique partially to the horizontal walls, also shows a negative drag reduction at the horizontal walls of $DR_{hor} = -2.38\%$ and a positive drag reduction of $DR_{ver} = 4.24\%$ at the side walls. The drag reduction of p:4.5 evaluated only at the inner section $-1.5 < z < 1.5$ yields an even larger drag increase of $DR_{hor,in} = -12.1\%$. This fact seems surprising and a more detailed analysis is needed.
These bar plots explain the different contributions of the side walls and the horizontal walls on the global drag reduction. However, they do not explain the cause of the relatively small and even negative drag reductions. Moreover, the cause for the drag increase of p:4.5 at the horizontal walls - even though d.4.5 shows drag reduction there - is not explained. Some further insights can be gained by looking at the distribution of the local wall shear stress along the horizontal and vertical walls. Figure 6.25 (a) displays the distribution of the wall shear stress τ_w along the horizontal wall at $-3 < z < 0$. Besides, figure 6.25 (b) shows the distribution of the RMS value of the fluctuating wall shear stress normalized by

$$\tau^+_{w,rms} = \frac{\tau'_{w,rms}}{\tau_w(z)}, \tag{6.1}$$

where $\tau_w(z)$ denotes the local wall shear stress at spanwise position z.
As previously, appropriate symmetries are used to improve the quality of the collected statistics. In order to be able to compare the results generated for the channel cases to the duct cases every case was normalized by the corresponding uncontrolled wall shear stress at the centre of the channel/duct $\tau^{z0}_{w,0}$. Hence, the wall shear stress for the uncontrolled duct case d:0 and for the uncontrolled channel case c:0 are 1 at the centre $z = 0$. Also a value of $\tau^+_{w,rms} = 0.37$ for the uncontrolled channel case is found which agrees with the classical value of $\tau^+_{w,rms} \approx 0.4$ put forward by Alfredsson et al. (1988). First, the reduction in τ_w and consequently the drag reduction for the channel cases c:4.5 and c:12 displayed in dashed lines is clearly visible.
The wall shear stress of the uncontrolled duct case along the horizontal wall rises from the corner to a small peak at $z \approx -2.75$, falls again to a minimum at $z \approx -2.3$ before

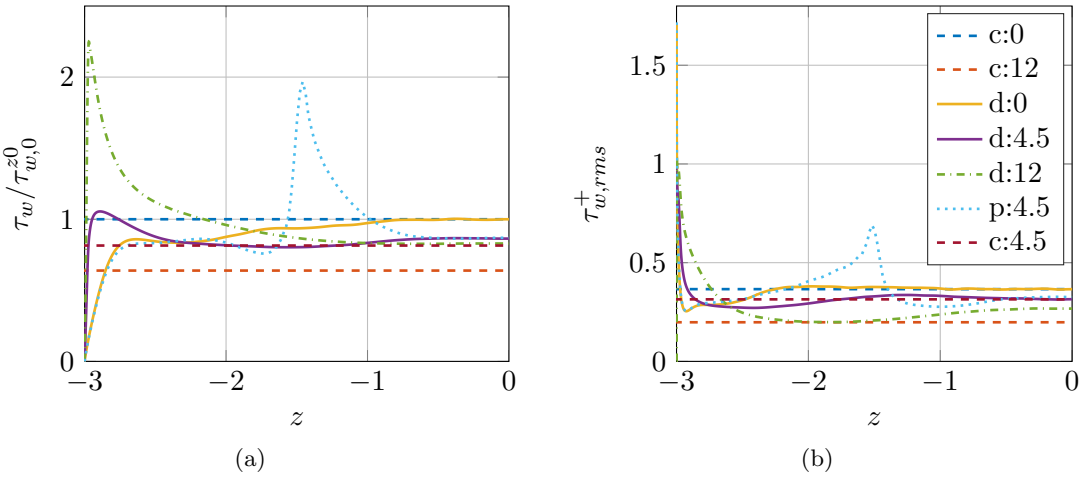

Figure 6.25.: Wall shear stress along the horizontal wall (a) and its RMS value (b).

it steadily rises to reach a constant level at $-0.8 \lesssim z < 0$. Its fluctuating value shows a significant peak at the corner $z = -3$ but soon reaches the classical value of 0.4.
The first peak of the controlled duct case d:4.5 is more pronounced than in d:0 and increased in magnitude. This peak is probably a result of the intensified streamwise vortex shown in figure 6.18 at the corner. This vortex convects high-speed fluid from the core region towards the corner, increasing the mean streamwise velocity close to the corner and consequently the wall shear stress at this location. This effect can already be observed in the 2D contour plot of the mean streamwise velocity in figure 6.2. Next to this peak, the expected effect of the control technique can be found. In a long region at $-2.3 \lesssim z < 0$ the wall shear stress is reduced compared to the uncontrolled case and is nearly constant. Thus, the average effect of the applied control technique is positive on the horizontal wall for case d:4.5.
At the centre of the duct the normalized wall shear stress of d:4.5 and c:4.5 are slightly different maybe due to a too short averaging time or because of remaining effects of the side walls. The fluctuating wall shear stress $\tau_{w,rms}^+$ is also reduced and agrees well with the corresponding value for the controlled channel c4.5 at the centre of the duct.

For the controlled duct case d:12 the first peak is much more pronounced and its negative effect on the averaged wall shear stress along the horizontal wall is unbalanced by the reduction in the centre of the duct at $-1.8 \lesssim z < 0$. Besides, the reduction in the centre of the duct is not nearly as good as for the corresponding channel case. This is probably also caused by the effect of the side walls.
The significant peak is probably formed by the strong streamwise vortex at the corner identified for this case in figure 6.18. Another mechanism not present in the uncontrolled duct is the fluid being pushed against the side walls by the oscillating horizontal walls. Due to conservation of mass this fluid is deflected in wall normal direction as can be seen in figure 6.4 and maybe also in streamwise direction accelerating U. This could also contribute to the strong peak located at $z \approx -3$ for the d:12 case.
A reduction in $\tau_{w,rms}^+$ for d:12 is visible in figure 6.25 (b) with a minimum at $z \approx -2$ agreeing with $\tau_{w,rms}^+$ of the corresponding c:12 case. However, in the centre the fluctuating wall shear stress for the d:12 case is again larger than that for the c:12 case.

The third controlled duct case p:4.5 also shows one significant peak the end of the controlled area $z \approx -1.5$. Apart from that peak and the adjoining region the distribution of τ_w coincides with d:0 in the uncontrolled region close to the corner and with d:4.5 in

the controlled region in the centre of the duct. The same is valid for the distribution of the fluctuating wall shear stress $\tau^+_{w,rms}$. The drag increase is solely caused by that peak which is much more pronounced than for the d:4.5 case. Furthermore, the deteriorated performance in the inner region $-1.5 < z < 1.5$ can be understood. The strongly increased wall shear stress at $-1.5 \lesssim z \lesssim -1$ is located inside the controlled region. It is not compensated by the drag reduction at $-1 \lesssim z < 0$ and consequently causes drag increase even at the controlled region $-1.5 < z < 1.5$. Moreover, the other region where positive drag reduction is achieved is located at $-2 \lesssim z \lesssim -1.5$ outside of the controlled region. Hence, drag reduction along the entire horizontal wall is more positive because that region at $-2 \lesssim z \lesssim -1.5$ is included and there are no detrimental effects at the corner.
One reason for this unproportionally strong peak is that the induced vortex is closer to the core region. The high-speed fluid which is convected towards the wall by that vortex, originates from a region of high mean streamwise velocity in the core of the duct. Another reason might be that the width of the rise and fall of the adjusted smoothed step function $\Delta\lambda$ described in section 4.2 is kept the same value $\Delta\lambda = 0.035$ for the p:4.5 case as for the other cases d:4.5 and d:12. However, the spacing between the grid points is much smaller at the corner and consequently the rise and fall of the smoothed step function is better resolved there. This might lead to a more abrupt stop of the control region causing a stronger disturbance at this location than at the corner. An indication that the generated streamwise vortex for the p:4.5 case is stronger than the one generated for the d:4.5 case is given by the increased maximum of kinetic energy of the secondary flow K_{max} of the p:4.5 case compared to the d:4.5 case. It would be interesting to study the effect of this parameter $\Delta\lambda$ on the applied control technique.

The distribution of the wall shear stress and its RMS value along the vertical walls is displayed in figure 6.26 (a) and (b). For the uncontrolled case d:0 two bumps are visible

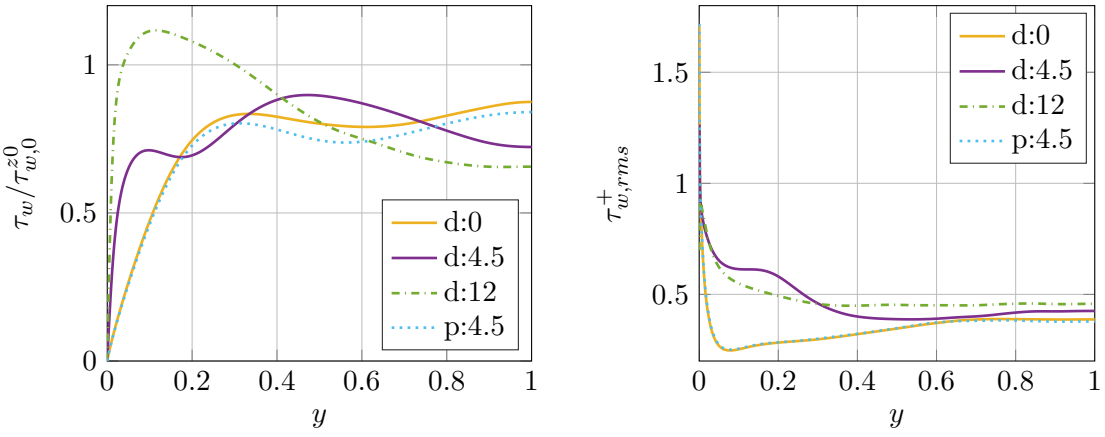

Figure 6.26.: Wall shear stress along the vertical wall (a) and its RMS value (b).

similar to the results presented by Gavrilakis (1992). The first controlled duct case d:4.5 again shows a peak close to the corner, a local minimum and maximum before a reduced wall shear stress level at $y = 1$ is reached. The reduced region around $y = 1$ is even increased for the second controlled duct case and is likely connected to the previously observed low-speed region of U in figure 6.2. Interestingly, the local minimum around $y = 0.2$ vanishes for the d:12 case and the maximum is still distinct but not as sharp and significant as along the horizontal wall. The p:4.5 case shows a slight reduction of wall shear stress along the whole vertical wall.
The fluctuating wall shear stress of d:0 and p:4.5 coincide along the whole vertical wall

and reach a value of $\tau^+_{w,rms} = 0.39$ again close to the classical value of 0.4. Unlike the behaviour along the horizontal wall the controlled cases d:4.5 and d:12 show an increased $\tau^+_{w,rms}$ even at $y = 1$ caused by the disturbance of the moving walls.

7. Conclusion and Outlook

The effect of harmonic wall oscillation on drag reduction and on the secondary flow patterns were investigated via direct numerical simulations. To the best of the author's knowledge, this is the first study where a flow control technique for turbulent drag reduction was tested in the duct geometry. However, a duct geometry is the natural choice for many laboratory experiments, with which DNS aims to compare. The present simulations allowed to address the discrepancy between numerical and experimental results observed by Gatti et al. (2015), the latter yielding less drag reduction. Besides, an investigation of the role of the secondary motions, as a possible cause of this discrepancy, was conducted.
In order to better understand the influence of different control parameters, four cases of the turbulent duct flow were simulated with the spectral element code Nek5000 (Fischer et al., 2008). One uncontrolled case was simulated and served as a reference. Two controlled cases, where both horizontal walls were almost completely oscillating were also simulated. They differ only in the chosen amplitude of wall velocity. In the third controlled duct case only the inner section of both horizontal walls was moved with the same amplitude of wall velocity as the lower one of the two other controlled cases.
The implementation was validated by comparing the results for one uncontrolled and one controlled channel case with data from the literature and data generated by a pseudo-spectral DNS code. The agreement between those was very good. Consequently, the duct flows are also considered to yield plausible results since they only differ in the applied boundary conditions.

All cases consistently show that there is a strong interaction between the spanwise wall velocity and the side walls, which can lead to severe detrimental effects. In some cases, in particular for the large spanwise oscillation amplitude, the effect of the side walls is not confined to their vicinity but extends into the core of the flow. The drag reduction is observed to be a local effect directly related to the local property of the spanwise Stokes layer as the very good agreement between the mean streamwise velocity profiles at the centre of the duct and in periodic channel flows show. However, this is only valid for small amplitudes of wall velocity. Additionally, the effects of the side walls on the flow close to them is clearly displayed in 2D contour plots. Mean wall-normal velocity and mean spanwise velocity show the formation of a strong streamwise vortex at the corner of the duct for the cases of almost completely moving walls, depicted in figure 7.1 (a). In the case of partially applied control a new pair of counter rotating streamwise vortices is generated at the lateral sides of the controlled region as depicted in figure 7.1 (b).

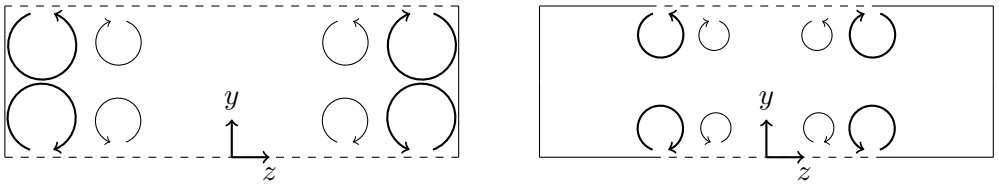

(a) (b)

Figure 7.1.: Schematic drawing of the induced streamwise vortices by the moving walls for (a) almost complete wall movement and (b) only inner section.

The RMS values of the fluctuating streamwise velocity show the expected reduction in the centre of the duct. However, they are strongly amplified at the side walls and at the lateral sides of the controlled region for the first two and the third controlled case respectively. This indicates already that the overall effect of the applied control technique will be inferior to the results in the channel case. The same behaviour at the side walls and at the end of the controlled region is also found for the RMS of wall-normal velocity fluctuations and the magnitude of the Reynolds stresses $\langle u'v' \rangle$, $\langle u'w' \rangle$, $\langle v'w' \rangle$.
Investigation of the secondary flow yielded that the wall movement strengthens the secondary flow, changes the shape of the classical pair of counter rotating streamwise vortices and their location. The controlled cases applying almost complete wall movement amplify one of the corner vortices which grows in size and pushes the other one closer to the centre of the duct. The new pair of counter rotating vortices for the third controlled case is clearly identified by streamline plots of the cross-stream motions.
The achieved levels of drag reduction in the duct compared to the channel are poor. Only the case of almost complete wall movement and the lower amplitude of wall velocity yields a positive global drag reduction of 3% compared to 19% in the channel case. The other controlled cases even show an increase in global drag. Further insights are obtained by splitting up the contributions of the horizontal walls and the vertical walls to the global drag reduction and by investigating the distribution of the wall shear stress along the horizontal and vertical walls. It is found that the region close to the corners and the region around the lateral sides of the controlled section are mainly responsible for the poor results regarding drag reduction in the current simulations of a turbulent duct flow.

The generated results raise new questions and further studies should be carried out to better understand the small or even negative achieved levels of drag reduction and the observed change of the secondary flow. One possibly important parameter is the width of the rise and fall of the implemented smoothed "step" function, $\Delta\lambda$, which was kept at one value for all the controlled duct cases in this thesis. This "step" function was used to smooth the transition between the uncontrolled and the controlled region of the horizontal walls. A large difference between the peak in the wall shear stress distribution of the case using partially moving walls and the one with almost complete wall movement and the same amplitude of wall velocity is found. This might be partially attributed due to a more abrupt end of the controlled section because of fewer grid points to resolve the smoothed rise and fall of the "step" function. Hence, a variation of this parameter and its impacts on the flow would be interesting.
Moreover, an investigation in a duct of higher aspect ratio, closer to the aspect ratio of the duct used in the experiment by Gatti et al. (2015), could help to clarify if there are still perceptible effects of the interaction between the applied control technique and the side walls on the measured level of drag reduction in the centre of the duct. The current results already suggest that the wall shear stress distribution along the horizontal wall is constant in a large region at the centre of the duct and almost as good as in the channel,

at least for not too high amplitudes of wall velocity, $W_m^+ = 4.5$. Furthermore, the available results could be used to formulate the estimated effect of the applied control technique on different combinations of aspect ratio and controlled region for $W_m^+ = 4.5$. Three assumptions could lead to such a model to predict the achieved drag reduction: wall shear stress being the same as in the uncontrolled case above the steady part of the walls, a constant drag increase at the end of the controlled section and a region of constant drag reduction above the moving walls. Such a model should be tested against experimental results and could be used to design further experimental investigations.
Two other modifications of the setup could be of interest. First, investigation of the secondary flow for a laminar controlled duct case could clarify the origin of the observed changes in the secondary motions of a turbulent duct flow. The observed features in the controlled turbulent duct flow might be simply a result of the harmonic oscillation of the walls and their formation would be consequently completely different to the Reynolds stress induced formation of the classical secondary motions in a duct. Finally, to better mimic the actuator used by Gatti et al. (2015), which was limited in length and width, a limitation of the controlled region not only in spanwise but also in streamwise length could be investigated.

Symbols and Abbreviations

Upper-case Roman

A	stiffness matrix
B	channel/duct width, mass matrix
C	constant in log law, convection matrix
C_f	skin friction coefficient
D	differentiation matrix
E	total number of elements
H	channel/duct height
K	kinetic energy of the secondary flow
$\langle K_{yz} \rangle$	K averaged over the whole cross section
$\langle K_{yz1} \rangle$	K averaged over the first window: $y \in [0, 2]$ and $z \in [-3, -2]$
Kn	Knudsen number
L	channel/duct length
$\mathcal{L}$	space of Lebesgue-square-integrable functions
L_N	Legendre polynomial of order N
P	mean pressure
P_w	mean pressure at the wall
Re	Reynolds number
Re_b	Reynolds number based on bulk velocity
$Re_{b,c}$	Reynolds number based on bulk velocity of the centre plane
Re_c	Reynolds number based on centreline velocity
Re_τ	Reynolds number based on friction velocity
$S(x)$	smoothed "step" function
U_b	bulk velocity
U_c	centreline velocity
U_j	j-component of the mean velocity
W_m	amplitude of the wall velocity
X^N	finite-dimensional trial space
Y^N	finite-dimensional test space

Lower-case Roman

c	convection velocity
f	body force
h	channel/duct half height
p	pressure
p'	fluctuating pressure
t	time
u	streamwise velocity, trial solution to Poisson equation
u_{ex}	exact solution to Poisson equation
u_j	j-component of the instantaneous velocity
u'_j	j-component of the fluctuating velocity
u_τ	friction velocity
v	wall-normal velocity, test function
w	spanwise velocity, arbitrary solution within the trial space X_0^N
x	cartesian coordinate, streamwise direction
x_j	j-component of cartesian coordinate
y	cartesian coordinate, wall-normal direction
z	cartesian coordinate, spanwise direction

Lower-case Greek

δ_{ij}	Kronecker delta
κ	von Kármán constant
λ	adjusted smoothed "step" function
$\Delta\lambda$	width of rise and fall of adjusted smoothed "step" function
ρ	density
μ	dynamic viscosity
ν	kinematic viscosity
ξ	coordinate on reference element
σ	stress tensor
τ	total shear stress
τ_w	wall shear stress
ω	oscillation frequency
Ω	whole problem domain
$\hat{\Omega}$	reference element

Upper-case Greek

Π	non-dimensional quantity
Φ	universal non-dimensional function
Ω	mean streamwise vorticity

Abbreviations

BDF3	third order backward differencing
CFR	constant flow rate
CPG	constant pressure gradient
CPU	central processing unit
DNS	direct numerical simulation
DR	drag reduction
EXT3	third order extrapolation
GLL	Gauss–Lobatto Legendre
NSE	Navier–Stokes equations
PDE	partial differential equation
RANS	Reynolds-averaged-Navier–Stokes
RMS	root-mean-square
SEM	Spectral Element Method

List of Figures

List of Tables

Bibliography

P. H. Alfredsson, A. V. Johansson, J. H. Haritonidis, and H. Eckelman. The fluctuating wall-shear stress and the velocity field in the viscous sublayer. *Physics of Fluids*, 31(5): 1026–1033, 1988.

A. Baron and M. Quadrio. Turbulent drag reduction by spanwise wall oscillations. *Applied Scientific Research*, 55:311–326, 1995.

D. Bechert, M. Bruse, W. Hage, J. v. d. Hoeven, and G. Hoppe. Experiments on drag-reducing surfaces and their optimization with an adjustable geometry. *Journal of Fluid Mechanics*, 338:59–87, 1997.

J.-I. Choi and H. J. Xu, C.-X.and Sung. Drag reduction by spanwise wall oscillation in wall-bounded turbulent flows. *AIAA Journal*, 40(5):842–850, 2002.

K. Choi. Near-wall structure of turbulent boundary layer with spanwise-wall oscillation. *Physics of Fluids*, 14(7):2530–2542, 2002.

K.-S. Choi, J.-R. DeBisschop, and B. R. Clayton. Turbulent boundary-layer control by means of spanwise-wall oscillation. *American Institute of Aeronautics and Astronoutics*, 36(7):1157–1163, 1998.

G. N. Coleman and R. D. Sandberg. A primer on direct numerical simulation of turbulence - methods, procedures and guidelines. Technical report, Aerodynamics & Flight Mechanics Research Group, School of Engineering Sciences, University of Southampton, 2010.

S. Corrsin. Turbulent flow. *American Scientist*, 49(3):300–325, 1961.

W. Couzy. *Spectral element discretization of the unsteady Navier–Stokes equations and its iterative solution on parallel computers*. PhD thesis, École Polytechnique Fédérale de Laussane, 1995.

M. O. Deville, P. F. Fischer, and E. H. Mund. *High-Order Methods for Incompressible Fluid Flow*. Cambridge University Press, 2002. ISBN 9780511546792.

P. F. Fischer, J. W. Lottes, and S. G. Kerkemeier. Nek5000: Open source spectral element CFD solver. available at `http://nek5000.mcs.anl.gov`, 2008.

J. Fish and T. Belytschko. *A First Course in Finite Elements*. John Wiley & Sons, Ltd, 2007.

K. Fukagata, K. Iwamoto, and N. Kasagi. Contribution of Reynolds stress distribution to the skin friction in wall-bounded flows. *Physics of Fluids*, 14(11):L73–76, 2002.

M. Gad-el Hak. *Flow Control – Passive, Active and Reactive Flow Management*. Cambridge University Press, Cambridge, 2000.

R. Garcia-Mayoral and J. Jimenéz. Drag reduction by riblets. *Philosophical Transactions of the Royal Society A*, 369:1412–1427, 2011.

D. Gatti, A. Güttler, B. Frohnapfel, and C. Tropea. Experimental assessment of spanwise-oscillating dielectric electroactive surfaces for turbulent drag reduction in an air channel flow. *Experiments in Fluids*, 56(5), 2015.

S. Gavrilakis. Numerical simulation of low-Reynolds-number turbulent flow through a straight square duct. *Journal of Fluid Mechanics*, 244:101–129, 1992.

F. Gessner and J. B. Jones. On some aspects of fully-developed turbulent flow in rectangular channels. *Journal of Fluid Mechanics*, 23:689–713, 1965.

D. Gottlieb and S. Orszag. *Numerical Analyses of Spectral Methods: Theory and Application*. SIAM-CBMS, Philadelphia, 1977.

W. Jung, N. Mangiavacchi, and R. Akhavan. Suppression of turbulence in wall-bounded flow by high-frequency spanwise oscillations. *Physics of Fluids*, 4:1605–1607, 1992.

J. Kim. Physics and control of wall turbulence for drag reduction. *Philosophical Transactions of the Royal Society of London A: Mathematical, Physical and Engineering Sciences*, 369:1396–1411, 2011.

J. Kim, P. Moin, and R. Moser. Turbulence statistics in fully developed channel flow at low Reynolds number. *Journal of Fluid Mechanics*, 177:133–166, 1987.

P. Kundu, I. Cohen, and R. Dowling. *Fluid Mechanics*. Elsevier, 5 edition, 2012.

F. Laadhari, L. Skandaji, and R. Morel. Turbulence reduction in a boundary layer by a local spanwise oscillating surface. *Physics of Fluids*, 6:3218–3220, 1994.

S. Lardeau and M. A. Leschziner. The streamwise drag-reduction response of a boundary layer subjected to a sudden imposition of transverse oscillatory wall motion. *Physics of Fluids*, 25(075109), 2013.

P. Luchini and M. Quadrio. A low-cost parallel implementation of direct numerical simulation of wall turbulence. *Journal of Computational Physics*, 211:551–571, 2006.

J. Malm, P. Schlatter, P. F. Fischer, and D. Henningson. Stabilization of the spectral element method in convection dominated flows by recovery of skew-symmetry. *Journal of Scientific Computing*, 57:254–277, 2013.

R. D. Moser, J. Kim, and N. N. Mansour. Direct numerical simulation of turbulent channel flow up to $Re_\tau = 590$. *Physics of Fluids*, 11(4):943–945, 1999.

H. Oertel jr., editor. *Prandtl - Führer durch die Ströemungslehre*. Springer Vieweg, 10th edition, 2012.

R. Örlü and P. Schlatter. Comparison of experiments and simulations for zero pressure gradient turbulent boundary layers at moderate Reynolds numbers. *Experiments in Fluids*, 54(6), 2013.

R. L. Panton. *Incompressible Flow*. John Wiley & Sons, Inc., Hoboken, New Jersey, 4th edition, 2013.

A. Patera. A spectral element method for fluid dynamics: Laminar flow in a channel expansion. *Journal of Computational Physics*, 54:468–588, 1984.

S. B. Pope. *Turbulent Flows*. Cambridge University Press, 7 edition, 2010.

L. Prandtl. Über die ausgebildete Turbulenz. In *Verh. 2nd Intl Kong*, NACA Tech. Memo 62, 2nd Intl. Kong für Tech. Mech., page 435, Zürich, 1926.

M. Quadrio. Drag reduction in turbulent boundary layer by in-plane wall motion. *Philosophical Transactions of the Royal Society of London A: Mathematical, Physical and Engineering Sciences*, 369(1940):1428–1442, 2011.

M. Quadrio and P. Ricco. Critical assessment of turbulent drag reduction through spanwise wall oscillations. *Journal of Fluid Mechanics*, 521:251–271, 2004.

P. Ricco, C. Ottonelli, Y. Hasegawa, and M. Quadrio. Changes in turbulent dissipation in a channel flow with oscillating walls. *Journal of Fluid Mechanics*, 700:77–104, 2012.

P. Schlatter and R. Örlü. Turbulent boundary layers at moderate Reynolds number: inflow length and tripping effects. *Journal of Fluid Mechanics*, 710:5–34, 2012.

H. Schlichting and K. Gersten. *Grenzschicht-Theorie*. Springer Berlin Heidelberg, 10 edition, 2006.

M. Skote. Turbulent boundary layer flow subject to streamwise oscillation of spanwise wall-velocity. *Physics of Fluids*, 23(081703), 2011.

J. H. Spurk. *Strömungslehre : Einführung in die Theorie der Strömungen*. Springer Berlin Heidelberg, 8th edition, 2010.

H. Tennekes and J. L. Lumley. *A First Course in Turbulence*. MIT Pres, 1972.

E. Touber and M. A. Leschziner. Near-wall streak modification by spanwise oscillatory wall motion and drag-reduction mechanisms. *Journal of Fluid Mechanics*, 693:150–200, 2012.

R. Vinuesa, A. Noorani, A. Lozano-Durán, G. K. El Khoury, P. Schlatter, P. F. Fischer, and H. M. Nagib. Aspect ratio effects in turbulent duct flows studied through direct numerical simulation. *Journal of Turbulence*, 15(10):677–706, 2014.

R. Vinuesa, P. Schlatter, and H. M. Nagib. Characterization of the secondary flow in turbulent rectangular ducts with varying aspect ratio. In *International Symposiom On Turbulence and Shear Flow Phenomena*, 2015.

P. R. Viswanath. Aircraft viscous drag reduction using riblets. *Progress in Aerospace Sciences*, 38:571–600, 2002.

A. Yakeno, Y. Hasegawa, and N. Kasagi. Modification of quasi-streamwise vortical structure in a drag-reduced turbulent channel flow with spanwise wall oscillation. *Physics of Fluids*, 26(085109):–, 2014.

J. Zierep and K. Bühler. *Grundzüge der Strömungslehre*. Springer Fachmedien Wiesbaden, 13 edition, 2013.

Appendix

The Appendix is used for some of the more complicated derivations which are not necessary to understand the main part.

A. Best fit property

In order to show that the trial solution $u(x)$ is the best one among all functions in the trial space X_0^N, an energy inner product and its induced norm are defined.

$$a(u,v) := \int_\Omega \frac{\mathrm{d}u}{\mathrm{d}x}\frac{\mathrm{d}v}{\mathrm{d}x}\mathrm{d}x = \int_\Omega (u)'(v)'\mathrm{d}x, \qquad \forall u,v \in \mathcal{H}_0^1 \tag{7.1}$$

$$||v||_a := \sqrt{a(v,v)}, \qquad \forall u,v \in \mathcal{H}_0^1 \tag{7.2}$$

In this context the $(\cdot)'$ denotes the first derivative.
With these definitions it will be shown that the deviation between the exact solution u_{ex} and an arbitrary solution w within the trial space X_0^N is greater or equal to the deviation between the exact solution and the approximate solution u (in terms of the previously defined norm). That is

$$||w - u_{ex}||_a \geq ||u - u_{ex}||_a, \qquad \forall w \in X_0^N. \tag{7.3}$$

This can be shown by substituting $v = w - u \in X_0^N$ into the left-hand side and using the definition of the norm 7.2 above

$$\begin{aligned}
||w - u_{ex}||_a^2 &= ||(v+u) - u_{ex}||_a^2 && (7.4)\\
&= ||v + (u - u_{ex})||_a^2 && (7.5)\\
&= \int_\Omega (v + (u-u_{ex}))'(v+(u-u_{ex}))'\mathrm{d}x && (7.6)\\
&= \int_\Omega (v)'^2 + 2(v)'(u-u_{ex})' + (u-u_{ex})'^2\mathrm{d}x && (7.7)\\
&= \int_\Omega (v')^2 + (u-u_{ex})'^2\mathrm{d}x && (7.8)\\
&\geq \int_\Omega (u-u_{ex})'^2\mathrm{d}x = ||u-u_{ex}||_a^2. && (7.9)
\end{aligned}$$

The second term in 7.7 vanishes because

$$\begin{aligned}
\int_\Omega (v)'(u-u_{ex})'\mathrm{d}x &= \int_\Omega (v)'(u)' - (v)'(u_{ex})'\mathrm{d}x && (7.10)\\
&= \int_\Omega (v)'(u)'\mathrm{d}x - \left[v(u_{ex})'\right]_{\partial\Omega} + \int_\Omega v(u)''\mathrm{d}x && (7.11)\\
&= \int_\Omega (v)'(u)' - \int_\Omega vf\mathrm{d}x && (7.12)\\
&= 0, \qquad \forall v \in X_0^N && (7.13)
\end{aligned}$$

The fact that v vanishes at the boundaries $\partial\Omega$ is used as well as the model problem 3.1 and its weak form 3.9.

B. Lagrangian interpolants

For a set of $N+1$ distinct points ξ_i Lagrangian basis polynomials $\phi_j(\xi)$ are constructed so that they are zero for all of the distinct points except one of the points. At this one point, their value is 1. More precisely, they satisfy the condition

$$\phi_j(\xi_i) = \delta_{ij}, \qquad 0 \leq i, j \leq N, \qquad \xi \in \hat{\Omega}. \tag{7.14}$$

Lagrangian basis polynomials can be written in a compact form as

$$\phi_j(\xi) := \prod_{\substack{i=0 \\ i \neq j}}^{N} \frac{\xi - \xi_i}{\xi_j - \xi_i}, \qquad 0 \leq j \leq N, \qquad \xi \in \hat{\Omega}. \tag{7.15}$$

This formula can be easily understood because the numerator vanishes for all $\xi = \xi_i$ except for $\xi = \xi_j$. For the latter case the result is one because the numerator and denominator are the same so the Kronecker delta condition 7.14 is satisfied. An equivalent form of equation 7.15 is given by

$$\phi_j(\xi) = \frac{\prod_{i=0}^{N} (\xi - \xi_i)}{(\xi - \xi_j) \prod_{\substack{i=0 \\ i \neq j}}^{N} (\xi_j - \xi_i)}, \qquad 0 \leq j \leq N, \qquad \xi \in \hat{\Omega}. \tag{7.16}$$

So the numerator is the polynomial of degree N with roots in ξ_i. The Gauss–Lobatto–Legendre (GLL) quadrature points are defined by

$$(1 - \xi^2) L'_N(\xi) = 0 = \prod_{i=0}^{N} (\xi - \xi_i), \qquad \forall \xi \in \hat{\Omega}, \tag{7.17}$$

where $L'_N(\xi)$ is the first derivative of the Legendre polynomial L_N of order N and ξ_i are the GLL points. Therefore, the numerator of equation 7.16 is simply $(1 - \xi^2) L'_N(\xi)$.
The first derivative of a polynomial $l(\xi)$ of degree N at one of its roots ξ_j can be given by

$$l(\xi) = \prod_{i=0}^{N} (\xi - \xi_i) \tag{7.18}$$

$$l'(\xi_j) = \prod_{\substack{i=0 \\ i \neq j}}^{N} (\xi_j - \xi_i), \qquad 0 \leq j \leq N, \tag{7.19}$$

which can be easily shown by using the product rule.
One part of the denominator in equation 7.16 is therefore identified as the first derivative of the numerator at one of its roots. The first derivative of the left-hand side of equation 7.17 is given by the definiton of the Legendre polynomials

$$-\frac{\mathrm{d}}{dx}\left((1 - x^2)\frac{\mathrm{d}}{dx} L_N(x)\right) = N(N+1) L_N(x), \qquad N = 0, 1, ... \tag{7.20}$$

Therefore, the denominator in equation 7.16 is $[-N(N+1)L_N(\xi_j)](\xi - \xi_j)$ and the Lagrangian interpolation polynomial of the Gauss-Lobatto-Legendre quadrature points is given by

$$\phi_j(\xi) = \frac{-1}{N(N+1)} \frac{(1 - \xi^2) L'_N(\xi)}{(\xi - \xi_j) L_N(\xi_j)}, \qquad 0 \leq j \leq N, \qquad \xi \in \hat{\Omega}. \tag{7.21}$$